CITY UNIVERSITY LONDON

EST 1894

City Research Online

Large-eddy simulation of ~~the flow over~~ two-dimensional dunes in a steady unidirectional flow

Mohammad Omidyeganeh and Ugo Piomelli*

Department of Mechanical and Materials Engineering, Queen's University, Kingston, Ontario, Canada K7L3N6

We performed large-eddy simulation of the flow over a typical two-dimensional dune geometry at laboratory scale (the Reynolds number based on the average channel height and mean velocity is 18,900) using the Lagrangian dynamic eddy-viscosity subgrid-scale model. The results are validated by comparison with simulations and experiments in the literature. The flow separates at the dune crest, generating a shear layer that plays a crucial role in the transport of momentum and energy, ~~as well as~~ the generation of coherent structures. The turbulent kinetic energy budgets show the importance of the turbulent transport and mean-flow advection in the bulk flow above the shear layer. In the recirculation zone and in the attached boundary layers, production and dissipation are the most important terms. Large, coherent structures of various types can be observed. Spanwise vortices are generated in the separated shear layer due to the Kelvin–Helmholtz instability; as they are advected, they undergo lateral instabilities and develop into horseshoe-like structures, are tilted downward, and finally reach the surface. The ejection that occurs between the legs of the vortex creates the upwelling and downdrafting events on the free surface known as "boils." Near-wall turbulence, after the reattachment point, is affected by large streamwise Taylor–Görtler vortices generated on the concave part of the stoss side, which affect the distribution of the near-wall streaks.

Keywords: large-eddy simulations; environmental turbulent flows; turbulent boundary layers

1.   Introduction

The flow over mobile sand beds in rivers has unique dynamics. Both the shape of the bed irregularities and their size influence the characteristics of the flow. When their dimensions become comparable to the water depth (the ratio of roughness to the depth is approximately $0.25 - 0.33$ [1, 2]), large-scale turbulent structures are generated that affect flow dynamics and sediment transport [3].

Among the most commonly found river-bed irregularities are dunes. A recent review of the dynamics of river dunes can be found in [4]; here, we only describe the fluid-dynamical features of dunes more relevant to this study. Dunes are created by small irregularities on a flat sand bed, which grow until a large-scale form is established. They ~~also~~ migrate in the flow direction and rarely reach an equilibrium shape, unless the flow is steady and unidirectional. However, an equilibrium state for the near-bed flow over developing dunes is

---

*Corresponding author. Email: ugo@me.queensu.ca

found by Coleman et al. [5] and it is shown by Venditti and Bauer [6] that flow characteristics are also the same for various flow conditions and dune geometries.

Generally, during the growth and movement of dunes, sand is lifted in the high-shear regions, and redeposited in the separated-flow area. Both this mechanism and bedload flux contribute to the formation of dunes. Dune formation may affect navigation, erosion of bridge piles and other structures, as well as dispersion of contaminants. Dunes also have a strong effect on channel drag and on the mechanisms of flow discharge in a river, especially during floods. The flow over a dune itself affects the bed deformation, sedimentation events, and has interactions with the free surface. Therefore, understanding the physics of the coherent motions present in this type of flow helps to understand the entrainment-deposition phenomena and bed formation. The strong interaction between the flow field, bed formation, and sediment transport phenomena emphasizes the need for comprehensive and collaborative research on flow simulation and bed deformation models, which are critical in geophysics and river engineering.

An experimental study on transition of bed forms from a flat shape into equilibrium large-scale dunes in unidirectional flow was conducted by Robert and Uhlmann [1]. As the flow velocity increases on a flat bed, the interaction between the flow and the mobile bed in a thick layer close to the bed creates two-dimensional ripple-like irregularities. Zones affected by sediment transport are extended to a much thicker region at higher discharge rates when irregular linguoid ripples are generated. These three-dimensional formations are transformed into two-dimensional dunes with increased average-flow velocity. At this time, the whole flow depth has been affected by sediment transportation. Initiation and development mechanisms of the irregularities that result in dune formation is also discussed by Coleman and Nikora [7].

Mean-flow characteristics reported in laboratory experiments [8–12], field observations [6, 13–15], and two-dimensional mathematical models [16, 17] reveal that the flow includes a recirculation zone and a shear layer due to the separation at the crest, an internal boundary layer after the reattachment on the stoss side, a wake region behind the recirculation zone, which extends toward the downstream dune, accelerating and decelerating flow on the stoss and lee side of dune, and an outer region near the surface. Despite the fact that various bed forms and Reynolds numbers were adopted, these characteristics of the mean flow and statistics were common [6]. Statistical measurements [8, 9] of turbulent flow over two-dimensional fixed bed forms revealed the fact that scaling velocity moments with local shear stress is inappropriate.

More detailed investigation on the turbulent structures were conducted using quadrant analysis [10]. Bennett and Best [10] concluded that Kelvin–Helmholtz instabilities in the shear layer are more likely to cause dune-related macroturbulence than turbulent boundary layer bursting, verifying the conclusions by Kostaschuk and Church [14].

Laboratory measurements of flow statistics and quadrant activities conducted across ripple-dune transition [2] revealed that turbulence production increases as the bed shape is changed from ripples to two-dimensional dunes and decreases afterward until three-dimensional dunes are formed. Over dunes, ejection events are more frequent but weaker than sweeps, although all four quadrants contribute to mass and momentum transport.

Recently, experimental studies of flow over three-dimensional bed forms showed significant changes of the flow field, compared with the flow over two-dimensional bed forms [18–20]. Secondary currents present in the flow significantly affect large-scale structures, and consequently alter the statistics. In addition, the flow dynamics are also strongly dependent on the three-dimensional shape of the bed.

One feature of the flow over dunes that has attracted significant attention is the variety of very large (with size comparable to the river depth) coherent structures that are observed. Several researchers have discussed these structures, and their role in the transport of mass and momentum. Best [12] observed boils (upwelling motions at the water surface, which usually occur when a horizontally oriented vortex attaches to the surface [21]) in a high-Reynolds-number flow over dunes in the laboratory and in the Jamuna River, Bangladesh, and proposed a schematic model for the interaction of coherent structures with the flow surface that results in boils. These general patterns of flow on the water surface over a dune-covered bed had been observed previously (see, for instance, [22] and other references cited in [4]) and are a dominant mechanism for sediment suspension [23, 24].

Wavelet analysis of field measurements [25] over the crest of a sand dune in Río Paraná in Argentina showed a strong correlation between the ejection events, caused by deceleration of flow on the lee side, and suspended sediments. Vortex shedding at the shear layer and wake flapping on the bed contribute to the formation of large-scale structures. The frequency of large turbulent events is related to the reattachment flapping events.

Analysis of the vorticity and velocity fields by Schmeeckle et al. [11] revealed coherent boil-like events similar to the boils observed in an open-channel flow over a smooth bed, but on a much larger scale (almost of the size of the flow depth). They observed spanwise rollers that grow in the separation region and later move downstream and begin to break up into smaller vortices. During this process, rollers transport material from the separation area into the flow interior and suspend a large amount of sediment grains. Their results show intermittent detachment of the near-bed spanwise vortices, which move toward the surface and are responsible for the boils.

Although the uniqueness of the structures that cause the boils in flows over dunes has been illustrated in laboratory measurements [4, 22, 26, 27] and field observations [28, 29], little is known of the generation, evolution, and distortion of these coherent structures. Several studies show that boil-generating structures start as a loop or horseshoe vortex [22, 27]. Best [4, 12] indicates that a vortex loop that touches the free surface causes the upwelling motion, that is, the boil. When the legs of the vortex loop attach to the surface, vertical vortices are generated.

Kadota and Nezu [27] suggest that the vortices generated at the shear layer have different morphology than those created after reattachment. They observed strong upward-tilting streamwise eddies, called "kolk structures," being generated at the reattachment point and rising to the surface. The spacing between kolks seemed to be narrower than that observed in previous experiments [14, 22, 26]. The periodicity of such strong upwellings has been investigated by Babakaiff and Hickin [28], who showed their wavelength to increase at low relative roughness (i.e., dune height to flow depth) and become constant when the ratio exceeds 0.2.

Discussion on the generation of large vortex loops that cause the strong upwelling at the surface is still inconclusive. Jackson [30] compared the frequency of bursting events and boils at the surface and concluded that boils are caused by these near-wall bursts. Müller and Gyr [22] proposed a mixing-layer analogy in which separated spanwise vortices at the crest undergo three-dimensional instabilities, which eventually cause hairpin-like vortices. The heads of these vortices are associated with low-speed fluid that rises up to the surface and generates boils. Their model is supported by visualization technique. Other authors [26, 27] identified vortices in the separated-flow region that move toward the reattachment point; they conjecture that kolk-boil vortices are formed due to oscillations of the reattachment line, similar to those that occur in the separated flow at a leading edge [31]; these vortices move to the surface and cause the boils. Kadota and Nezu [27]

performed flow visualization and conditional sampling at very low Reynolds numbers to support this argument. There are also qualitative descriptions of the mechanism in which vortex loops are generated [4, 11, 12] that essentially conform to one of the above models.

The flow over river dunes has also been studied numerically, by the solution of the Reynolds-averaged Navier–Stokes (RANS) equations [32, 33] and large-eddy simulations (LES) [34–37]. We concentrate on LES, since RANS solutions are unable to capture the turbulent eddies that are the focus of the present work. Large-eddy simulation of turbulent flow and sediment transport over large-scale ripples were carried out by Zedler and Street [38]. They solved an advection–diffusion equation for the sediment transport that is sufficiently accurate at low concentrations, but neglected the interaction of the sediment with the flow. They observed the lifting of sediment in high shear-stress regions that move downstream and upward.

Yue et al. [34] performed LES of the flow over typical two-dimensional dunes using a level-set function to account for the free-surface deformation. Periodic boundary condition in streamwise and spanwise directions were applied. The domain had length $L_x = 20h$ and width $L_z = 7h$, where h is the dune height. Two flow depths at the crest were simulated: $6.6h$ and $3.24h$, denoted as deep and shallow flows; the Reynolds number (based on the flow depth and the surface streamwise velocity at the crest) was 58,000 and 10,700 for the two cases, respectively. In general, the first- and second-order statistics were in good agreement with the experiments by Balachandar et al. [39]. The simulations showed upward-tilted vortices close to the free surface in the shallow flow. Compared to the deep-flow simulation, more small-scale structures were present on the surface of the shallow flow, which gave the appearance of roughness at the free surface. The results showed that the interaction of the free surface and the flow structures is significantly affected by the flow depth. The same authors subsequently performed LES in nearly the same configuration, and visualized periodically flapping spanwise rollers in the recirculation zone [35].

Stoesser et al. [36] also performed LES of flow over dunes with parameters similar to those used by Yue et al. [35]: the dune wavelength was $20h$, the maximum depth was $4h$, and $Re = 25,000$ based on maximum depth and average bulk velocity. The first- and second-order statistics agreed well with the experiments in the literature. The simulations showed rollers at the crest that expanded to the size of the dune height as they were convected toward the reattachment point. A few instantaneous snapshots of spanwise vorticity and velocity vectors highlighted the upward movement of vortices after the reattachment point. They concluded that the boils on the surface were originally hairpin eddies generated in the reattachment region as a result of secondary instabilities of rollers that are elongated in the streamwise direction and tilted upward. However, the instantaneous visualizations of velocity fluctuations do not show a strong upwelling at the surface, but rather a structure more similar to the smaller, weaker boils that occur at the surface of open-channel flows over flat surfaces [40].

More recently, Grigoriadis et al. [37] performed LES of the flow in the geometry studied experimentally by Kadota and Nezu [27]. The dune wavelength was $20h$ and the maximum flow depth was $4h$. Two cases were studied, with Reynolds numbers (based on average flow depth and mean bulk velocity) equal to 17,500 and 93,500. They examined the turbulent eddies in more detail than previous investigators. Their results, however, differ somewhat from previous experimental and numerical observations: in their simulations the horseshoe structures did not reach the surface. They, however, observed kolk vortices generated by the interaction between streamwise vortices that reach the dune crest from upstream and

185 rollers generated at the crest. Kolk vortices were found to last for long times, and were the most significant structures observed at the surface in their simulations.

Despite the experimental and numerical investigations of this problem, several questions remain open: what are the large structures in the flow and why are they different in the experiments and simulations? Are the large-scale structures at the surface generated in

190 the shear layer or in the attached region? What are the statistics and dynamics of these structures? How do they interact with the surface? Another feature of interest in these flows, and one that has been studied considerably less frequently, is the near-wall turbulence structure. Are the near-wall eddies similar to those that occur in other canonical wall-bounded flows, or are they affected by separation, reattachment, curvature of the bed, and

195 pressure gradient that occur on the upward-sloping surface (the "stoss" side)? The present work tries to answer some of these questions. We focus on the dynamics of the large-scale and near-wall coherent structures to understand their signatures.

In the following, we begin by presenting the problem formulation and the numerical method used. Then, in Section 3, mean-flow statistics are compared with previous ex-

200 periments and simulations in the literature to validate this work; then the large coherent structures at the surface and the near-wall turbulence are investigated in more details. Concluding remarks and recommendations for future work will end the article.

2. Problem formulation

In LES, the velocity field is separated into a resolved (large-scale) and a subgrid (small-

205 scale) field by a spatial filtering operation [41]. The nondimensionalized continuity and Navier–Stokes equations for the resolved velocity field are

$$\frac{\partial \overline{u}_i}{\partial x_i} = 0, \tag{1}$$

$$\frac{\partial \overline{u}_i}{\partial t} + \frac{\partial \overline{u}_i \overline{u}_j}{\partial x_j} = -\frac{\partial \overline{P}}{\partial x_i} - \frac{\partial \tau_{ij}}{\partial x_j} + \frac{1}{Re_b} \frac{\partial^2 \overline{u}_i}{\partial x_j \partial x_j}, \tag{2}$$

where $Re_b = U_b H_b / \nu$, H_b is the average channel depth, and U_b is the average velocity at the location of average depth. x_1, x_2, and x_3 are the streamwise, wall-normal and spanwise directions, also referred to as x, y, and z. The velocity components in these directions are,

210 respectively, u_1, u_2, and u_3 (or u, v, and w). An overline denotes a filtered quantity, and $\tau_{ij} = \overline{u_i u_j} - \overline{u}_i \overline{u}_j$ are the subgrid stresses, which were modeled using an eddy-viscosity assumption

$$\tau_{ij} - \delta_{ij} \tau_{kk}/3 = -2\nu_T \overline{S}_{ij} = -2C\overline{\Delta}^2 |\overline{S}| \overline{S}_{ij}. \tag{3}$$

Here, $\overline{\Delta} = 2(\Delta x \Delta y \Delta z)^{1/3}$ is the filter size, $\overline{S}_{ij} = (\partial \overline{u}_i/\partial x_j + \partial \overline{u}_j/\partial x_i)/2$ is the resolved strain-rate tensor and $|\overline{S}| = (2\overline{S}_{ij}\overline{S}_{ij})^{1/2}$ is its magnitude. The coefficient C is determined

215 using the dynamic model [42] with the Lagrangian averaging technique proposed by Meneveau et al. [43], and extended to non-Cartesian geometries by Jordan [44] and Armenio and Piomelli [45].

The governing differential Equations (1) and (2) are discretized on a nonstaggered grid using a curvilinear finite-volume code. The method of Rhie and Chow [46] is used

220 to avoid pressure oscillations. Both convective and diffusive fluxes are approximated by second-order central differences. A second-order-accurate semi-implicit fractional-step
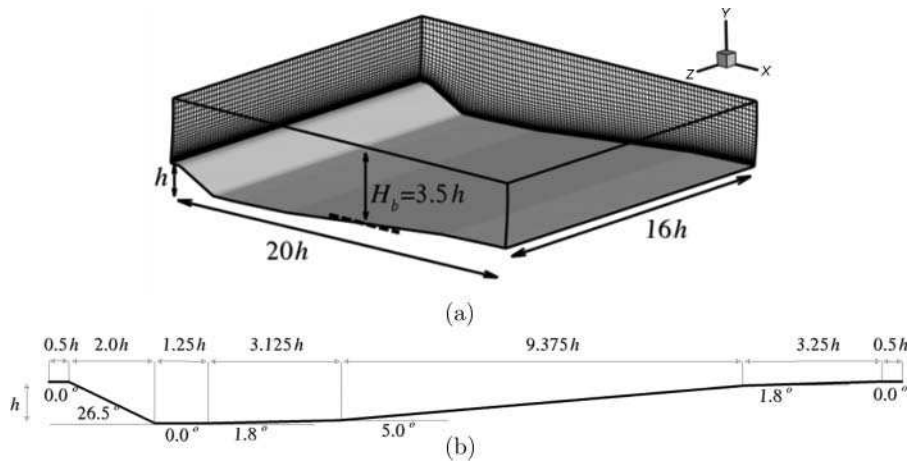
Figure 1.   (a) Sketch of the physical configuration (every fourth grid line is shown), and (b) bed geometry.

procedure [47] is used for the temporal discretization. The Crank–Nicolson scheme is used for the wall-normal diffusive terms, and the Adams–Bashforth scheme for all the other terms. Fourier transforms are used to reduce the three-dimensional Poisson equation into a series of two-dimensional Helmholtz equations in wavenumber space, which are solved iteratively using the BiConjugate Gradient Stabilized method. The code is parallelized using the Message-Passing Interface and the domain-decomposition technique, and has been extensively tested for turbulent flows [48–51].

Dunes are known to reach a periodic equilibrium shape [30, 52] in the case of steady unidirectional flows, with a wavelength equal to 5 or 6 times the flow depth, and height equal to 1/4 of the flow depth. For this reason, most dune shapes studied experimentally and numerically are quite similar. We use the geometry studied by Balachandar et al. [52] and Stoesser et al. [36]. The computational configuration is sketched in Figure 1. Periodic boundary conditions are used in the streamwise (x) and spanwise (z) directions. The flow is driven by a pressure gradient that maintains a constant flow rate in time. The free surface is assumed to be rigid and free of shear stress: the wall-normal velocity is set to zero, as are the vertical derivatives of the streamwise and spanwise velocity components. The surface deformation is reported to be small (less than 2.0% of the flow depth) in experiments [9, 18, 27] and simulations [35, 36]. Therefore, the free-slip condition is expected to have small effects on the statistics and on the evolution of significant structures. The Reynolds number is 18,900 based on the channel average height and average velocity at the cross section with height h.

An orthogonal mesh is generated using a hyperbolic grid-generation technique. The resolution of the basic simulation is the same as that used by Stoesser et al. [36], but the computational domain is twice as wide as that used in that study; thus, the number of points used is $416 \times 128 \times 384$, twice as many as those used in [36]; the grid spacings in local wall units are $\Delta s^+ \approx 12.9$ (streamwise), $\Delta z^+ \approx 6.0$ (spanwise), and $0.1 < \Delta n^+ < 12.1$ (wall normal). Note that the grid spacings above are comparable to those used in many Direct Numerical Simulations of the Navier–Stokes equations. A grid-sensitivity analysis was performed with resolutions of $240 \times 96 \times 200$, $416 \times 128 \times 384$, and $640 \times 180 \times 640$,
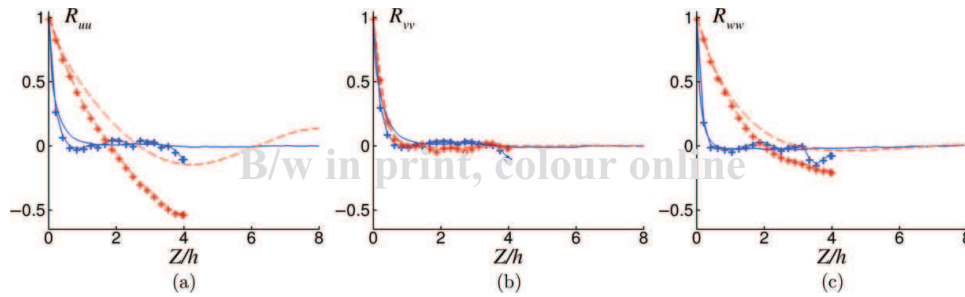
Figure 2.   Spanwise velocity autocorrelation function at two points in the x–y plane $(15h, 1h)$ and $(15h, 3.75h)$; ——— close to the wall; – – – close to the surface; the lines correspond to the wide domain, lines and crosses to the narrow one. (a) R_{uu}, (b) R_{vv}, and (c) R_{ww}.

and grid convergence of the statistics was verified: first- and second-order statistics were within 5% of each other for all resolutions. Only the results obtained with the intermediate grid resolution are shown in the following.

Since this study focuses on the larger flow structures, we examined the spanwise autocorrelation function

$$R_{\alpha\alpha}(r) = \frac{\langle u'_\alpha(x, y, z)u'_\alpha(x, y, z + r)\rangle}{\langle u'_\alpha(x, y, z)u'_\alpha(x, y, z)\rangle} \tag{4}$$

(where $u'_i = \overline{u_i} - \langle\overline{u_i}\rangle$ are the velocity fluctuations, $\langle\cdot\rangle$ represents an average in time and spanwise direction, and no summation is implied over Greek indices) to ensure that the domain width was sufficient to include the largest structures at the surface. This quantity is shown in Figure 2 for a calculation that used the same domain width as [36], and for one that is twice as wide. While the near-wall eddies can be resolved adequately by a smaller domain, a domain of at least $8h$ is necessary to allow the development of the larger coherent structures at the surface. As a result, we employed a computational domain that is twice as wide as that used in [36], and four times as wide as that employed by [37].

The equations were integrated in time for $100h/U_b$ time units to remove transient effects. Then statistics were accumulated over $1000h/U_b$ time units. To increase the sample size, averaging was also performed in the spanwise direction. To verify the adequacy of the sample, we compared statistics obtained using only half of the sample with those obtained using the complete sample, and found that the mean velocities differed by less than 0.1%, and the r.m.s. intensities by less than 0.5%.

3.   Results

3.1.   *Mean flow*

The accuracy of the simulations was first verified by a grid-refinement study and by comparing statistics with simulation and experiment reported by Stoesser et al. [36]. Figure 3 shows contours of averaged streamwise velocity, $\langle\overline{u}\rangle$, wall normal velocity, $\langle\overline{v}\rangle$, pressure, $\langle\overline{p}\rangle$, and Reynolds shear stress, $-\langle u'v'\rangle$. The flow separates at the dune crest and reattaches downstream on the bed, creating a recirculation region. The pressure contours show a favorable pressure gradient that accelerates the flow over the stoss side (the upward-sloping region for $x > 8h$) and an unfavorable gradient for $x < 8h$. Due to the separation of the
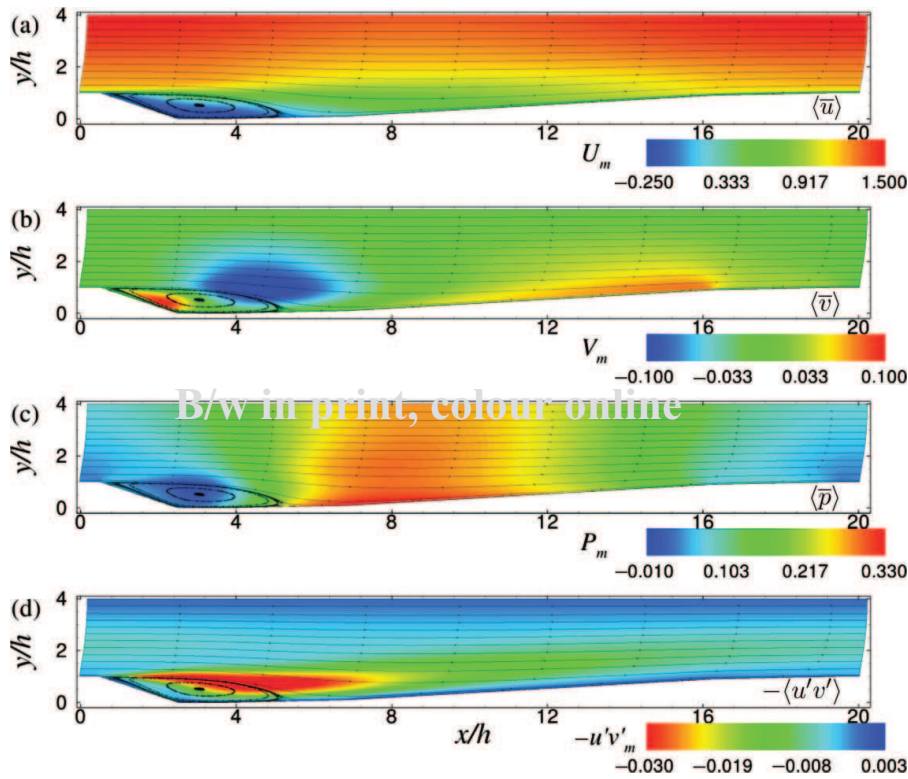
8   *M. Omidyeganeh and U. Piomelli*

Figure 3.   Contours of the average (a) streamwise velocity, $\langle\overline{u}\rangle$, (b) wall normal velocity, $\langle\overline{v}\rangle$, (c) pressure, $\langle\overline{p}\rangle$, and (d) Reynolds shear stress, $-\langle u'v'\rangle$.

flow, a shear layer is generated after the crest that expands ~~in the wake region~~ toward the next dune.

In Figures 3 and 4(a), streamlines are shown to visualize the averaged recirculation zone in the lee side. Comparison between this simulation and the literature, as well as the results of the grid refinement study, are shown in Figure 4.(a) The velocities are normalized with the bulk velocity at the last vertical line in Figure 4(a). Excellent agreement is obtained with the previous simulation, and between meshes, indicating that the intermediate grid results are fine enough for convergence of statistics. Note that, as mentioned in the paper by Stoesser et al. [36], the experimental data is not reliable in the wake area due to some inconsistencies in the measurements (mass conservation is not satisfied). Also in Figure 4(c), the Reynolds shear stress is compared along six vertical lines specified in Figure 4(a). Overall good agreement is obtained with experiments and with the simulation by Stoesser et al. [36].

Figure 5 shows the streamwise development of the wall stress τ_w and the acceleration parameter

$$K = \frac{\nu}{U_\infty^2}\frac{dU_\infty}{dx}, \qquad (5)$$

as well as profiles of mean velocity and $q^2 = \langle u_i'u_i'\rangle$ (twice the turbulent kinetic energy (TKE)) at several locations on the stoss side. Quantities denoted by a plus are normalized
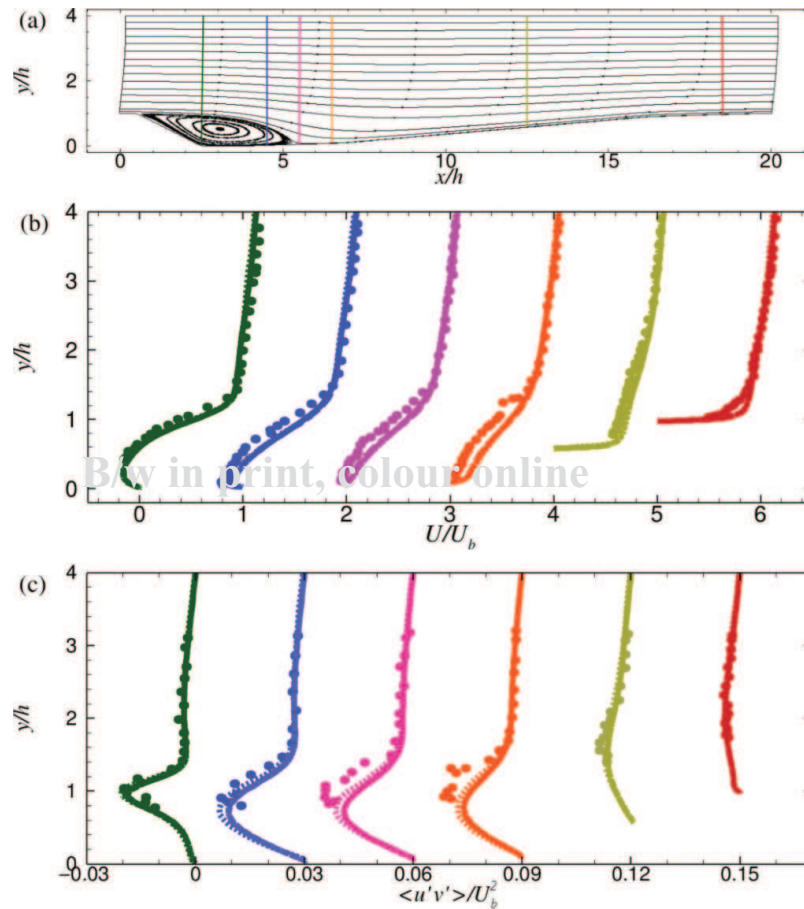
Figure 4.   (a) Average streamlines; the vertical lines indicate the position of the profiles in (b) and (c), from left to right: $x/h = 2.5, \ 4.5, \ 5.5, \ 6.5, \ 12.5, \ 18.5$; (b) streamwise velocity profiles; (c) profiles of Reynolds shear stress. Each profile is shifted to the right for clarity. —— Present simulation, intermediate mesh; $---$ present simulation, fine mesh; $\cdots$ LES [36]; • experiment by Polatel cited in [36].

using the viscosity ν and the local friction velocity (calculated at the same x location as the lines) $u_\tau = (\tau_w/\rho)^{1/2}$, and $y^+ = yu_\tau/\nu$. The wall shear stress becomes negative immediately downstream of the crest. Note the localized peaks that correspond to discontinuities in the slope of the dune. The acceleration parameter shows a region of adverse pressure gradient (from the dune crest to $x/h \simeq 9$) followed by a favorable pressure-gradient region. K never reaches the critical value where the flow is expected to begin to relaminarize [53], $K_{crit} \simeq 2.75 \times 10^{-6}$. For the values of K encountered on the stoss side, the pressure-gradient effects are not expected to be large, and the flow is dominated by the reattachment, and recovery toward equilibrium.

The average reattachment point is at $x/h \simeq 5.7$, close to the value predicted by Stoesser et al. [36], and in the range of other experiments and simulations [27, 37] ($x/h \simeq 4 - 6$), but smaller than the backward-facing step and separation bubble experiments [54, 55]. This is due to the convergence of the flow on the stoss side of the dune and the associated
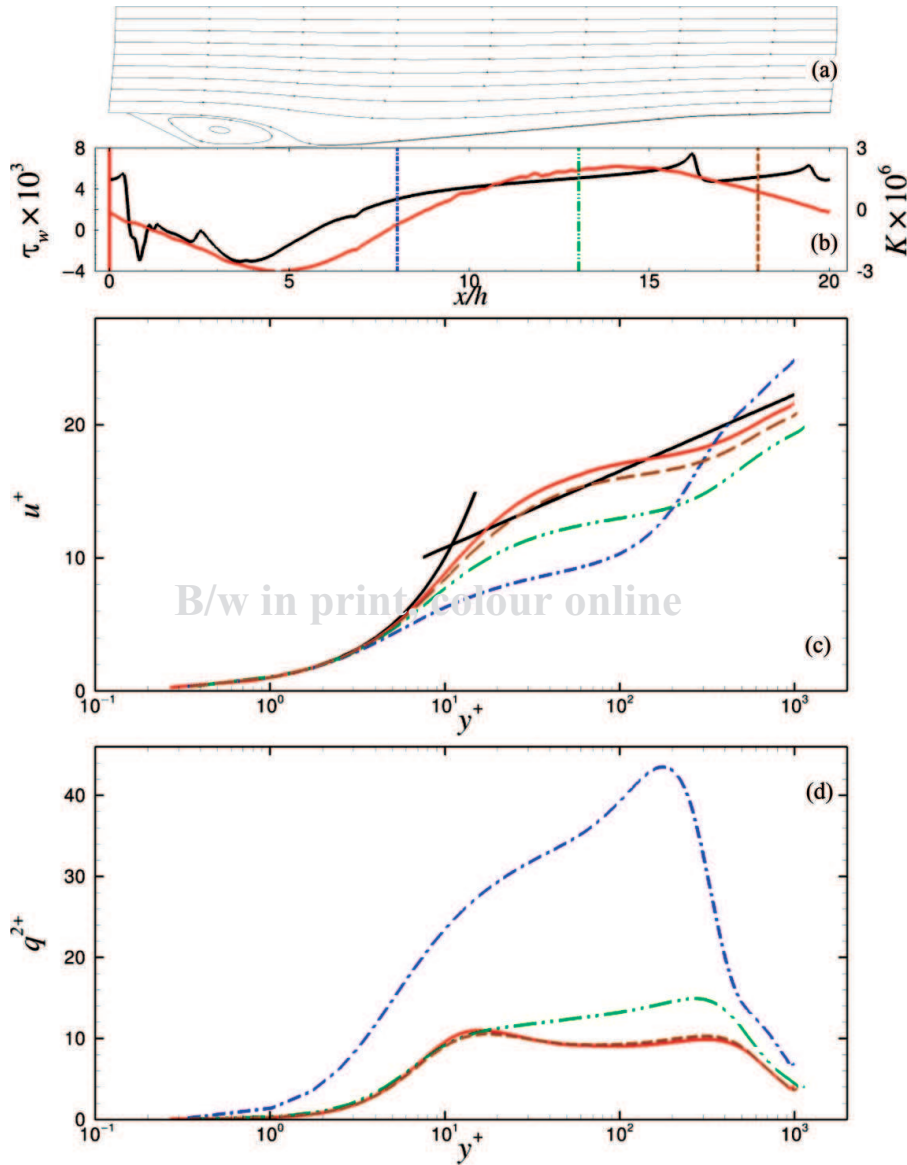
Figure 5.   (a) Mean-flow streamlines; (b) ——— wall stress τ_w and ——— acceleration parameter K; (c) mean velocity profiles in wall units on the stoss side and on the dune crest; (d) profiles of q^2 in wall units on the stoss side and on the dune crest. The profiles are taken at the locations shown by vertical lines in part (b) ($x/h = 0, 8, 13, 18$).

favorable pressure gradient result. Shortly after the reattachment, the wall stress is still very low, and the TKE is dominated by the free shear layer, which causes an outer-layer peak. Further downstream the velocity profiles take the shape also observed in the recovery region downstream of a backward-facing step (see Figure 19 in [56]). The recovery of the logarithmic layer appears, however, faster than in the backward-facing step, perhaps because of the flow acceleration. At $x/h \simeq 13$ we observe a two-layer structure in the

profile of q^2: the outer-layer peak due to the shear layer is still dominant, but an inner layer
is beginning to be reestablished, with a near-wall peak of TKE. By $x/h \simeq 18$ the outer
peak has been damped, while the inner one has reached the value and location ($q^{2+} \simeq 12$
at $y^+ = 16$) typical of attached boundary layers. Note, however, that even at the dune crest
some remnant of the detached shear layer can be observed (the contours of the Reynolds
shear stress shown in Figure 3(d) also present the same feature), indicating that the effect
of the separation is felt over distances longer than the dune wavelength, and that the flow
in one dune is affected by the separation in the preceding one.

3.2. *Turbulent kinetic energy budgets*

The transport equation for the resolved TKE is

$$0 = -U_j \frac{\partial k}{\partial x_j} + \mathcal{P} + \mathcal{T} + \Pi + \mathcal{D} + \varepsilon, \tag{6}$$

where

$$\mathcal{P} = -\langle u_i' u_j' \rangle \frac{\partial U_i}{\partial x_j}, \tag{7}$$

$$\mathcal{T} = -\frac{\partial}{\partial x_j} \left[\frac{1}{2} \langle u_i' u_i' u_j' \rangle + \langle u_i' \tau_{ij}' \rangle \right], \tag{8}$$

$$\Pi = -\frac{1}{\rho} \left\langle u_i' \frac{\partial p'}{\partial x_i} \right\rangle, \tag{9}$$

$$\mathcal{D} = \frac{2}{Re_b} \nabla^2 k, \tag{10}$$

$$\varepsilon = -\nu \left\langle \frac{\partial u_i'}{\partial x_j} \frac{\partial u_i'}{\partial x_j} \right\rangle + \left\langle \frac{\partial u_i'}{\partial x_j} \tau_{ij}' \right\rangle, \tag{11}$$

are the production, turbulent transport, pressure transport, viscous diffusion, and dissipation,
respectively.

Figures 6 shows the terms in TKE budget, normalized by U_b^3/h. Almost all terms are
important in the wake and shear layer generated as a result of the separation of flow at the
crest, while dissipation and production are the most important terms in the attached-flow
regions. The mean-flow advects energy from the shear layer toward the wall, and also toward
the downstream dune. Due to a large streamwise velocity gradient around the reattachment
point, the production term is negative there. A region with negative turbulent transport is
located between two regions with positive transport, one near the wall and the other near
the bulk flow. This behavior was also observed in the separated region of the flow in an
S-shaped duct by Silva Lopes et al. [49]. A positive and a negative region of turbulent
transport extend toward the downstream dune; the positive region also extends to the free
surface. Pressure transport and viscous diffusion are not as strong as other mechanisms,
although they are more significant in the shear layer. Pressure transports energy from the
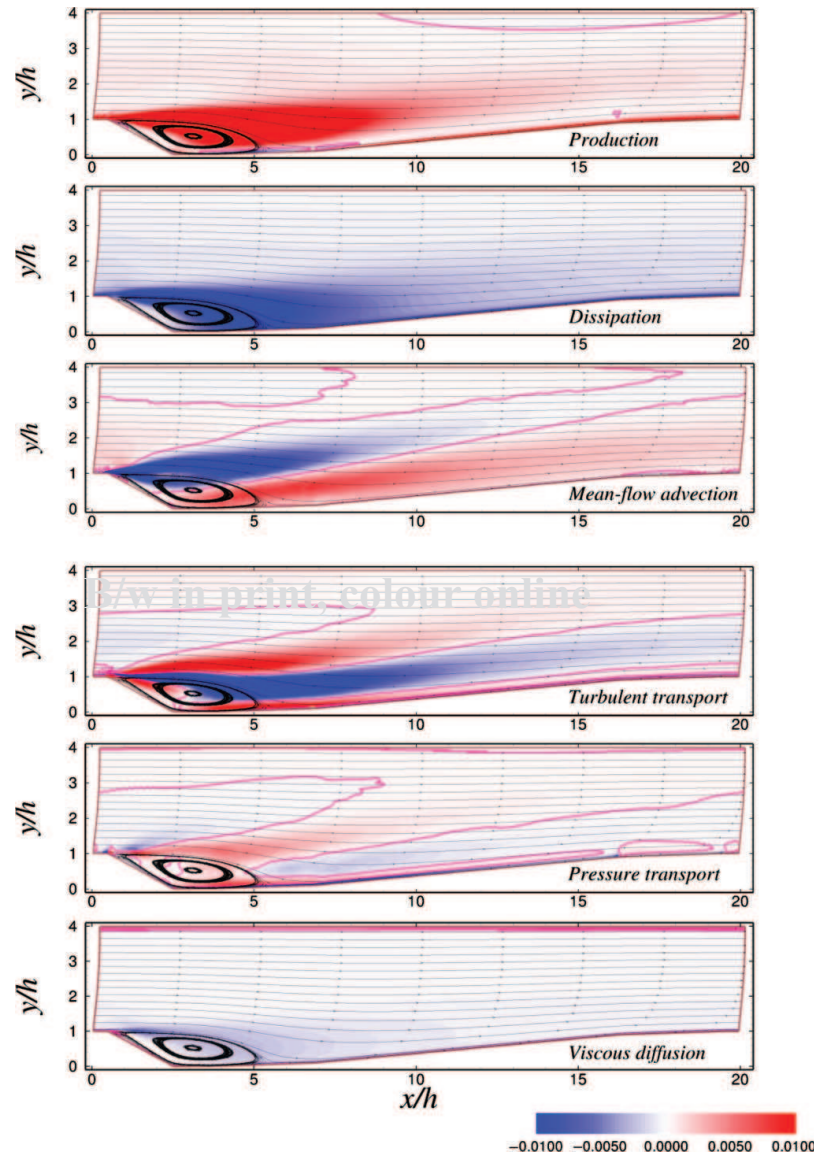outer layer to the inner layer around the reattachment point.

Figure 6.   Turbulent kinetic energy budgets: production, dissipation, mean-flow advection, turbulent transport, pressure transport, and viscous diffusion terms; mean-flow streamlines and the zero contour line are shown by black and magenta lines, respectively.

3.3.   *Turbulence structure*   340

Figure 7 shows contours of streamwise velocity fluctuations u' on a plane close to the wall, comparing the flow behavior on the dune with that in an open channel with a flat bed. The latter has the well-known structure of attached wall-bounded flows, with alternating low- and high-speed streaks. The dune shows a rather different behavior. First, the separation zone on the lee side of the dune is characterized by large, spanwise-oriented eddies (similar 345 to those observed in a backward-facing step by Le et al. [56]). Second, instead of alternating
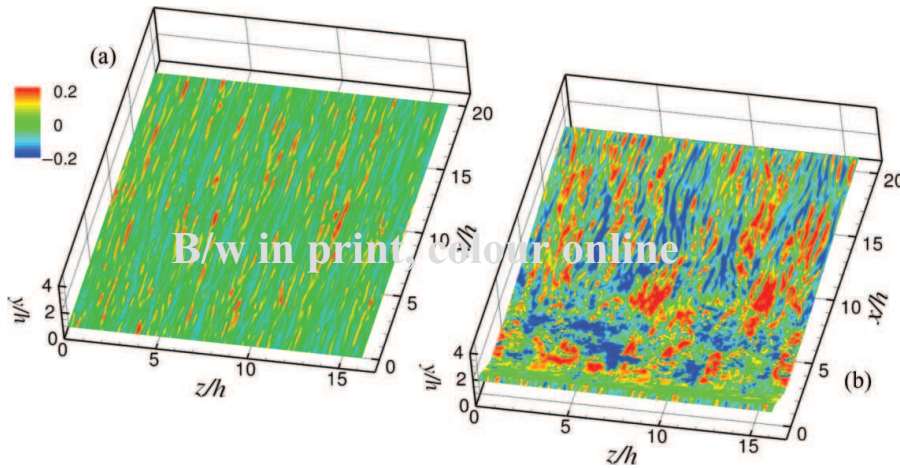
Figure 7.   Contours of streamwise velocity fluctuations on a plane parallel to the bed five wall units away from the solid wall. (a) Open channel; (b) dune.

high- and low-speed streaks, we observe streamwise-oriented stripes of low-speed streaks alternating with stripes of high-speed ones. This pattern is due to the presence of large longitudinal vortices on the stoss side of the dune. To visualize these structures, we show, in Figure 8 the secondary-flow streamlines and contours of wall-normal velocity fluctuations. These quantities were averaged over a short time, approximately $20h/U_b$, to visualize better the large vortices, which tend to meander. We clearly observe very large structures, of the order of the flow depth. At least two pairs of counter-rotating vortices are present on average, and are similar to the structures that have been observed in experimental and numerical studies of the flow over concave surfaces [57–59]. The size of these eddies is of the order of the flow depth, similar to what was observed in the flow over smooth wavy channel [60] and hills [61].

The two-point spanwise correlations on the stoss side, shown in Figure 9 for the streamwise and wall-normal velocity components (again averaged over a short time only), also show the signature of these large structures, as well as the streaky structures in the near-wall region. Near the wall R_{vv} has a negative minimum, similar to the canonical boundary layer behavior, and reflecting the effect of the quasi-streamwise vortices (the
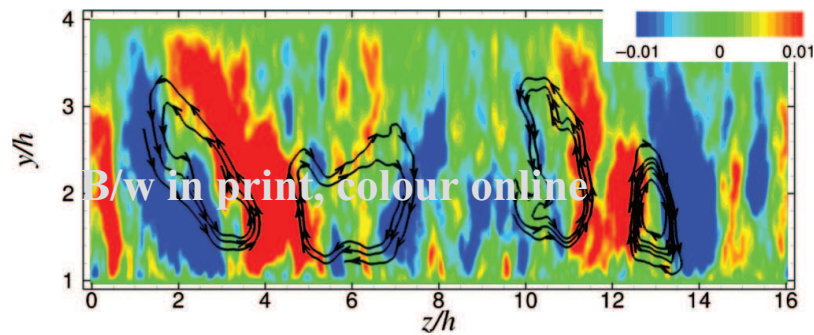

Figure 8.   Secondary-flow streamlines in the y–z plane at $x = 15h$, superposed on the contours of short time-averaged wall-normal velocity fluctuations.
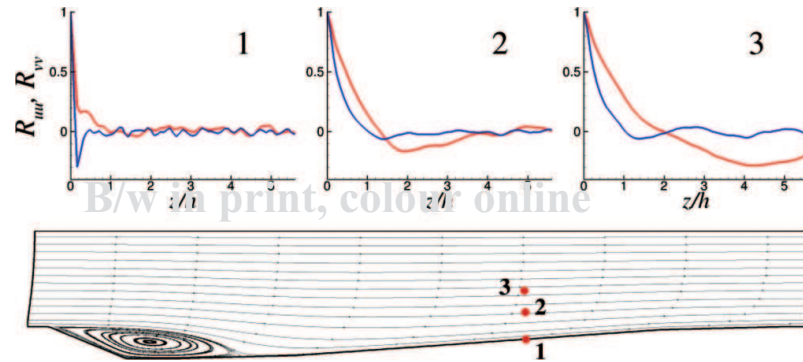
Figure 9.   Spanwise auto-correlations at three points on the stoss side at $x/h = 12.8$. —— R_{uu}; —— R_{vv}.

point where the minimum occurs corresponds to half of the streak spacing [62]). R_{uu}, on the other hand, shows the structure typical of flows with two distinct length scales, in a ratio of approximately 4:1. Away from the wall the longitudinal vortices result in a negative peak of the spanwise autocorrelation, which occurs for a separation $z/h = 4$, corresponding to the two vortex pairs observed in Figure 8.

Figure 10 shows the outer-layer structures at an instant in time. Spanwise vortices are generated in the shear layer separating from the crest due to the Kelvin–Helmholtz instability. They are convected downstream and either interact with the wall or rise to the surface, taking the form of large horseshoe-like structures. These structures may undergo an intense distortion, become one-legged, or be completely destroyed. The region behind the head (and between the legs) of horseshoe vortices is generally characterized by an intense Q2 event (where $u' < 0$ and $v' > 0$), as shown in Figure 11, where the velocity fluctuation vectors in a x–y plane are also shown. Initially (Figure 11(a)), small ejections occur after the crest that results in the generation of a small spanwise vortex, which grows as it is advected downstream (Figure 11(b)). It also becomes three-dimensional, taking a hairpin-like shape (Figures 11(b) and (c)). As it grows to dimensions comparable to (or
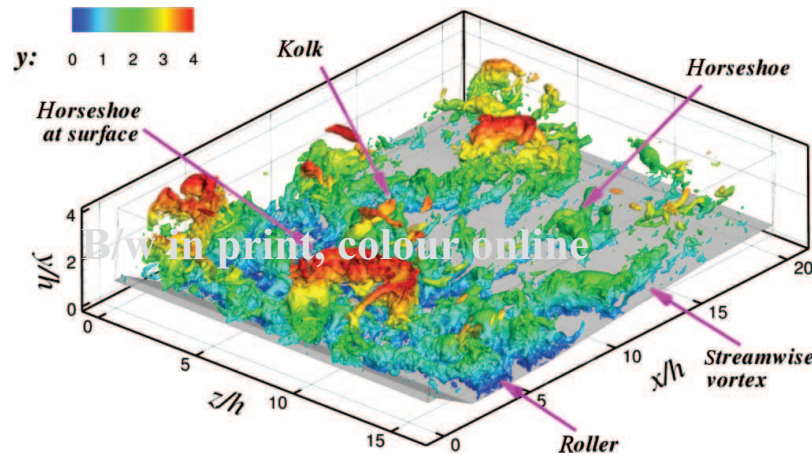

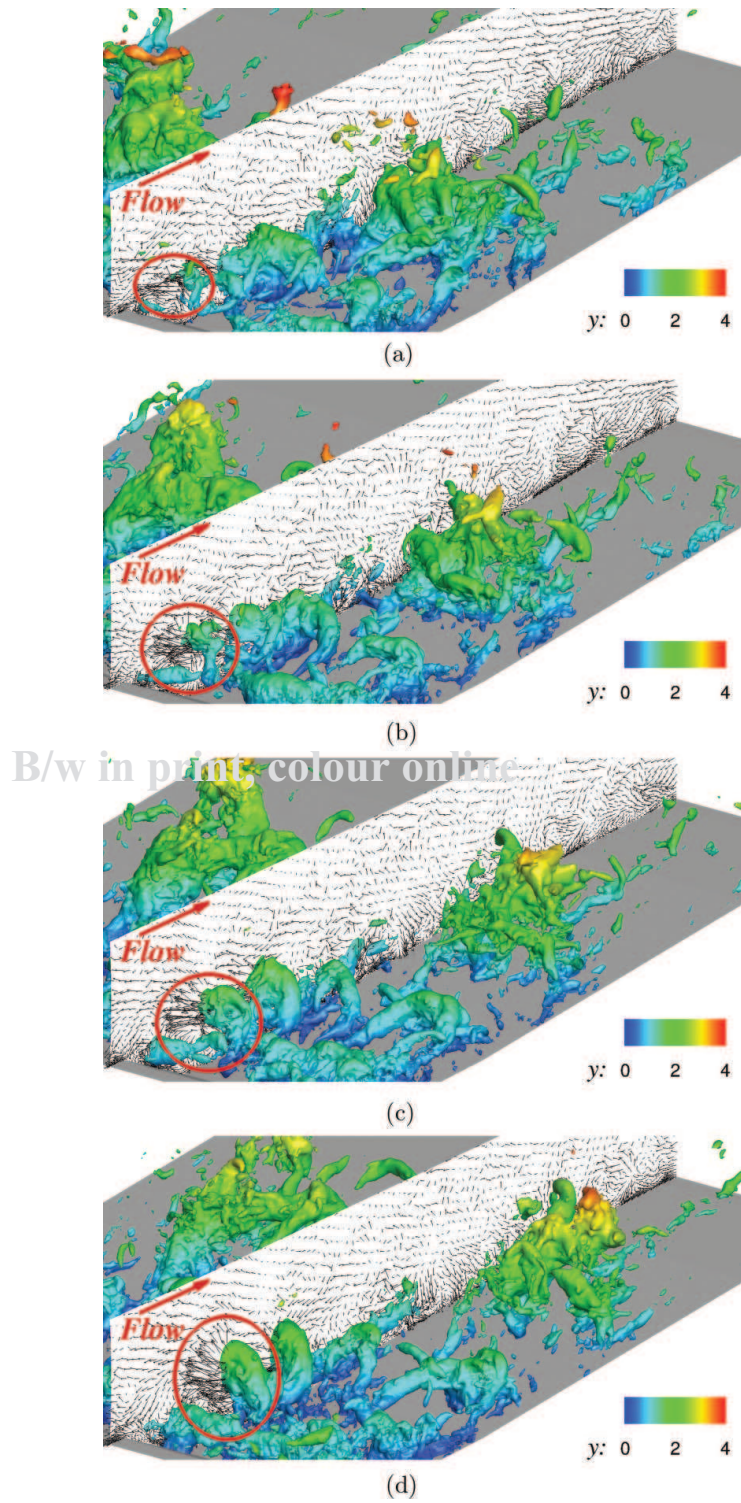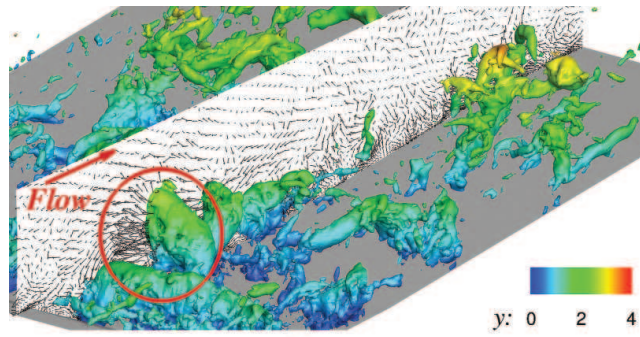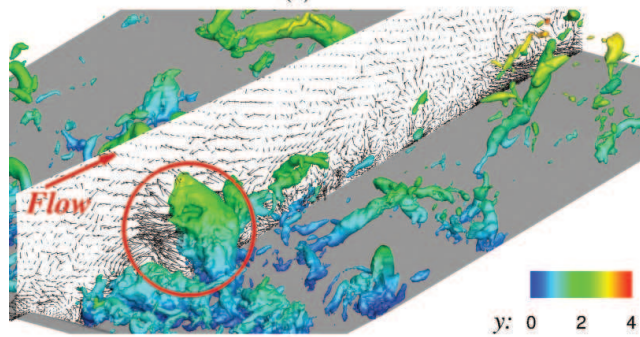Figure 10.   Instantaneous isosurfaces of pressure fluctuation colored with height.

Figure 11. Evolution of a large horseshoe structure; the time interval between snapshots is $1.5h/U_b$; vectors of velocity fluctuations are shown on a vertical plane at $z = 10.7h$ for every five grid points.
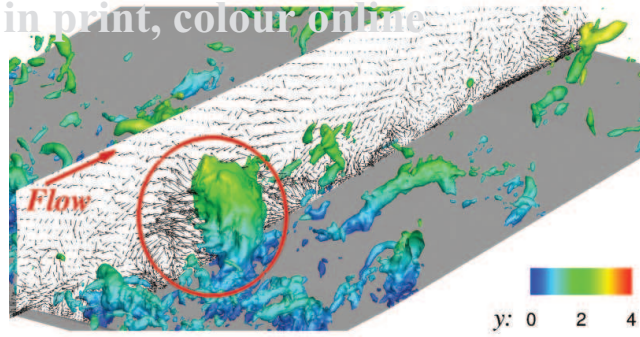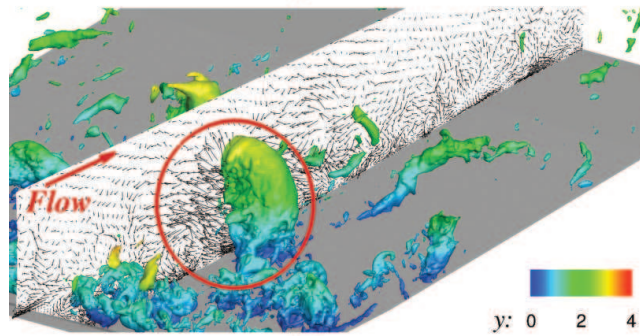
(e)

(f)

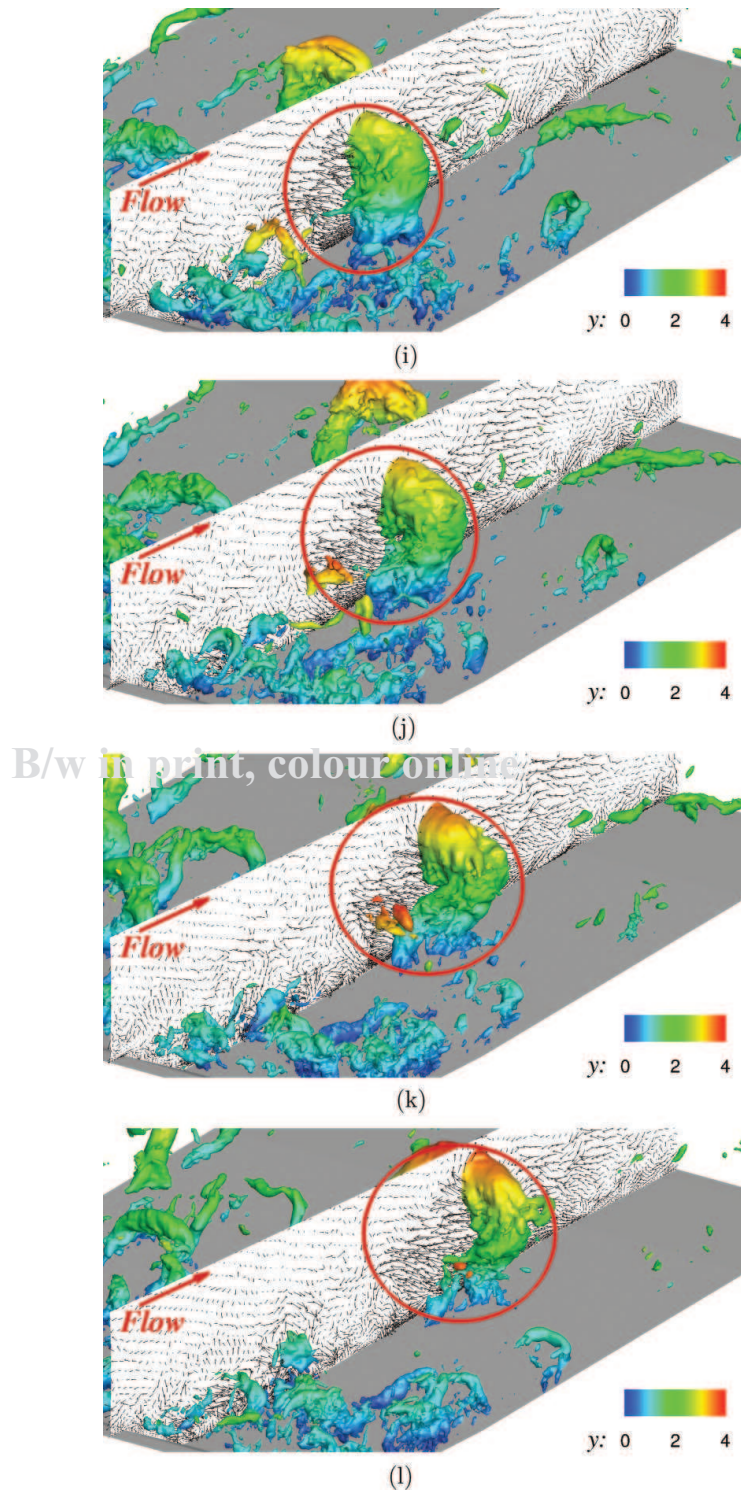B/w in print, colour online

(g)

(h)

Figure 11.   (Continued).

(i)

(j)

B/w in print, colour online

(k)

(l)

Figure 11.   (Continued).

larger than) the flow depth, a strong ejection occurs between the legs (Figure (c)). When
interacting with other vortices, it may merge with them (Figure 11(d) and (c)), or destroy them. If the structure survives it becomes larger and rises up along the shear layer (Figures 11(d)–(l)).

As illustrated in Figure 12, the same structure is elongated and tilted downward as it rises to the surface; eventually its tip touches the surface. This development is similar to that observed for horseshoe vortices in open-channel flow over a smooth bed, where Q2 events happen between the vortex legs, while Q4 events ($u' > 0$ and $v' < 0$) are found outside the legs [63]. The vortex is originally vertical (see Figure 11), but is later tilted downward (see Figure 12) forming an angle between $40°$ and $60°$ with respect to the x–z plane (Figure 13). The signatures of Q2 and Q4 events are also illustrated by the three-dimensional vectors on the inclined plane in this figure.

As the vortex loop is convected downstream it becomes elongated and distorted. Its legs reach the surface, creating an upwelling, which expands and weakens. Figure 14 shows pressure-fluctuation isosurfaces at four instants. Since the tip of the structure is distorted faster, in the last image it is no longer visible with the p' value used. The legs of the vortex loop remain coherent for a longer time, and generate vertical vortices around the boundaries of the boil. This surface behavior was also observed by Best [12] in field and laboratory observations at larger Reynolds numbers.

As mentioned before, among the most characteristic events due to the coherent structures in the flow over dunes are the boils, upwelling motions at the water surface. Since in the present calculation the free-surface is rigid, we cannot observe true upwelling motions. We can, however, still identify boil-like events through various surrogate quantities. First, we considered the pressure: since the boil occurs due to an upward motion, which in this calculation is limited by the rigid surface, we expect boils to be accompanied by significant positive pressure fluctuations p'. Second, by continuity the upwelling motion resolves into lateral motions on the surface; thus, the planar part of the velocity-fluctuation divergence, $\partial u'/\partial x + \partial w'/\partial z$, is expected to be large and positive. The fluctuating velocity vectors in the free-surface plane are also expected to be oriented radially from the center of the boil. Finally, the TKE $\mathcal{K} = \langle u_i' u_i' \rangle/2$, is expected to be large at the edge of the boil where the flow downdrafts (appearing as surface waves in observations by Best [12]). In Figure 15, we show contours of these quantities on the free surface, at a time corresponding to Figure 14(b). We observe a region of negative p' where the head of the horseshoe vortex contacts the surface and, immediately upstream of the contact point, the positive p' region associated with the impingement region. Consistent with the expected behavior, the planar divergence and $\mathcal{K}$ are large, and the velocity vectors are oriented radially.

If we compare the signature of boils in the flow over dunes with that over a smooth bed (Figure 16), we observe the same qualitative features; the signature of the boils is, however, stronger for the dune flow (the values of pressure and TKE, and the vector magnitudes are higher in the dune geometry). Furthermore, at the surface of the open-channel flow over the smooth bed, the size of the boils that develop is smaller than for the flow over dunes: much larger and stronger boils are generated by the large horseshoe-like structures present when water flows over dunes (Figure 17). Over a hundred snapshots, covering almost $400h/U_b$ time units, have been observed for both geometries in order to examine the size of these events at the surface. Consistent with experimental observations [11], we find that in the dune case these events may be larger than the flow depth ($\sim 8h$ in Figure 17), while when the bed is smooth they are at most in the size of the boils shown in Figure 16(d) ($\sim 3h$).

We conclude that, while all the criteria above can be used, the pressure fluctuations (with the positive value identifying the center of the boil) and the divergence of the velocity
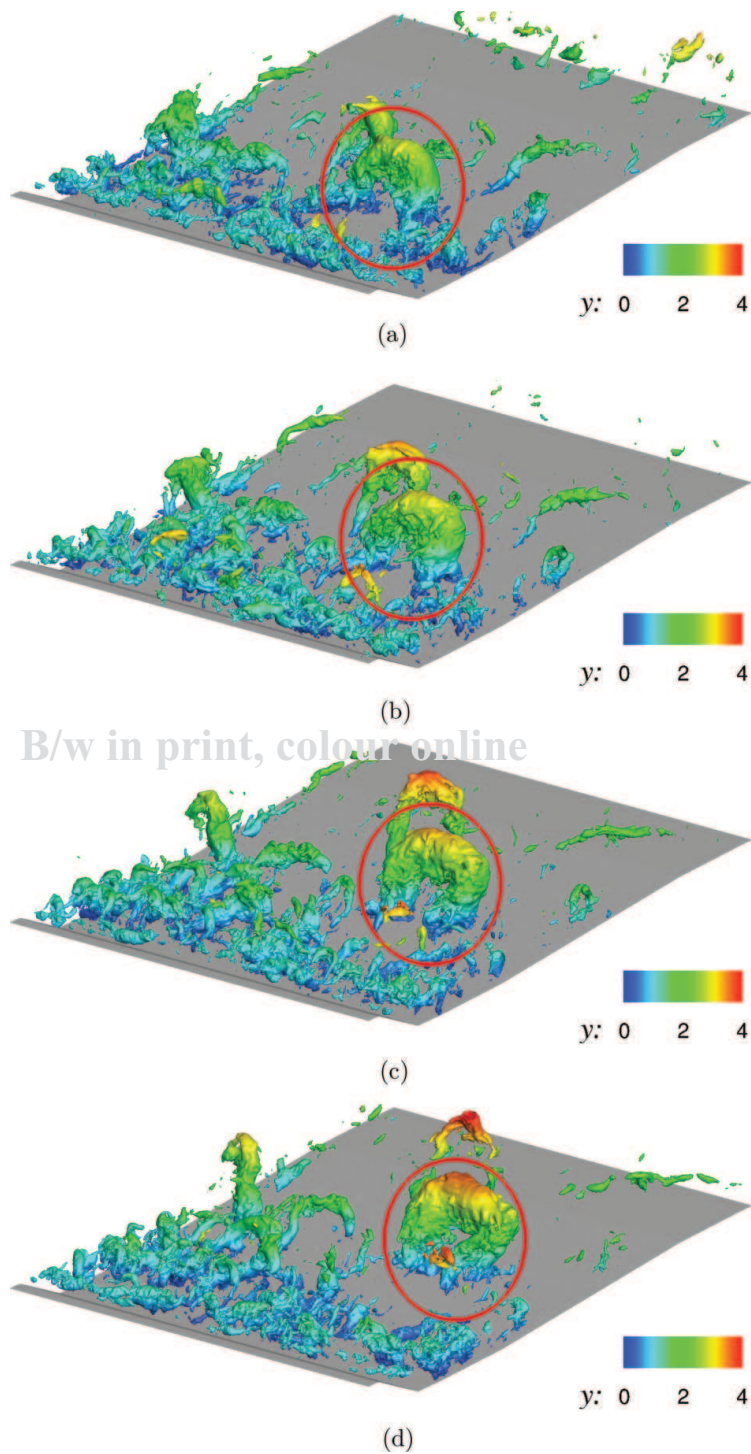
Figure 12. Convection of a large horseshoe structure downstream; the time interval between snapshots is $1.5h/U_b$; these snapshots are at the same instants as Figures 11(h)–11(l), except for the last one, (f), which occurs $1.5h/U_b$ time units after (e).
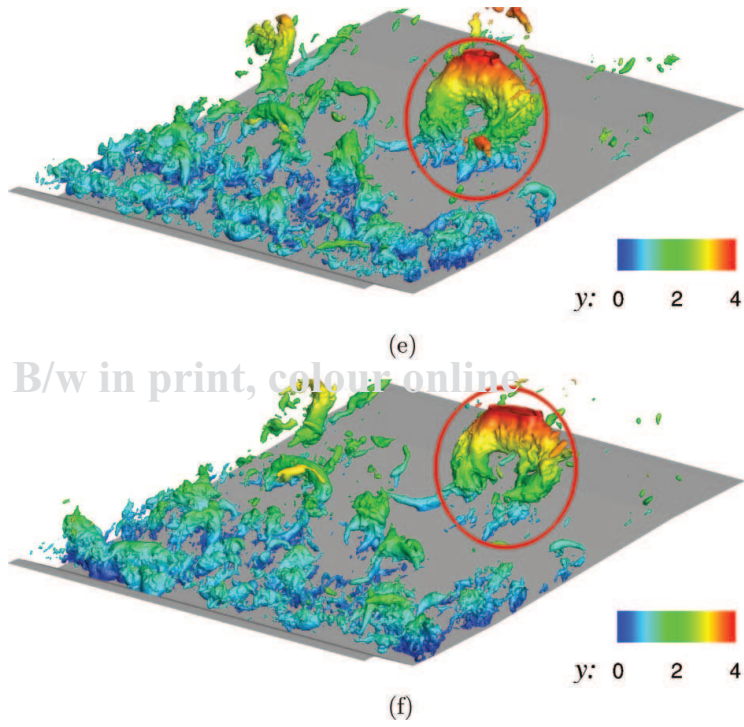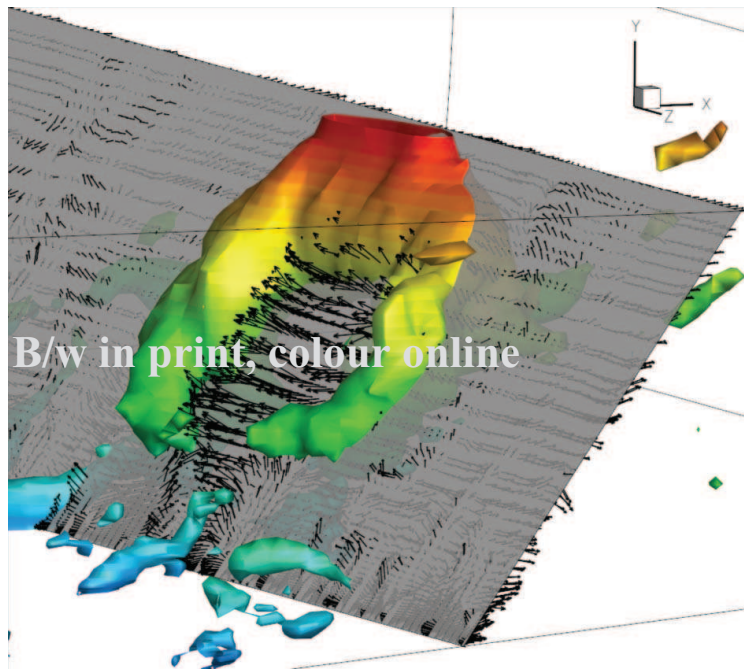
Figure 12.   (Continued).

Figure 13.   Visualization of the flow near a large horseshoe structure when it touches the surface.
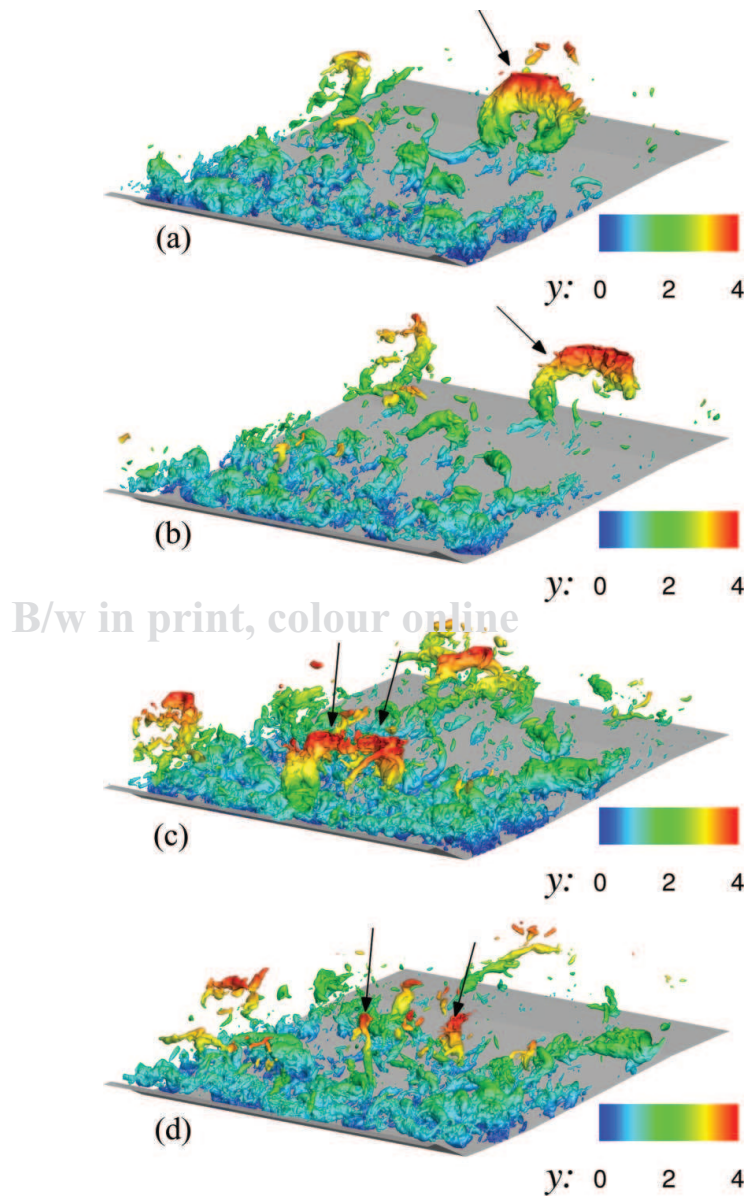
Figure 14. Interaction of the vortex loop with the free surface. The time step between snapshots is $3h/U_b$. The first snapshot is $3h/U_b$ later than the instant in Figure 13. The horseshoe vortex indicated by an arrow in (a) and (b) is reintroduced into the domain by the periodic boundary conditions in (c) and (d). Pressure isosurface levels are $p' = -0.08$ in (a) and (b), -0.06 in (c) and -0.04 in (d).

vectors are the most reliable identifiers. We use a threshold $p' > 0.08$, chosen from an exam of the probability density function (PDF) and cumulative density function (CDF) of the pressure at the surface averaged over the entire free surface and time (shown in Figure 18), which shows that this criterion identifies only the strongest pressure events at the surface.
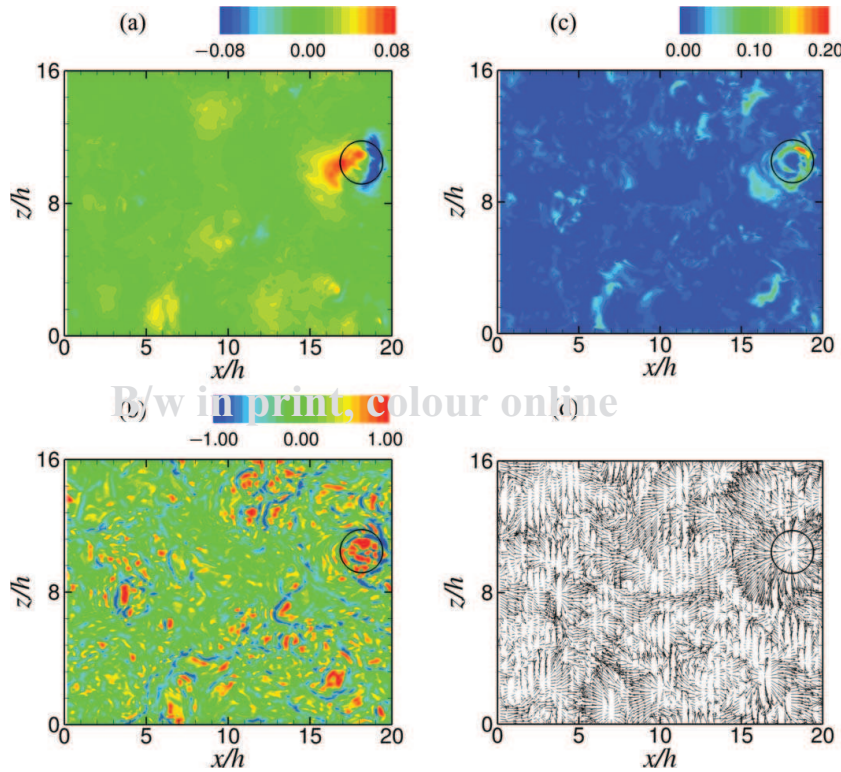
Figure 15. Identification of a boil at the surface of flow over dune bed using (a) pressure fluctuations p', (b) planar fluctuating velocity divergence $\partial u'/\partial x + \partial w'/\partial z$, (c) turbulent kinetic energy $\mathcal{K}$, (d) fluctuating velocity vectors.

Based on the considerations above, we identified a boil as a connected region in which the fluctuating pressure is greater than 0.08. We considered 10,000 flow realization, covering a total time $1000h/U_b$ (50 flow-through times), and observed boils in 50% of the fields considered. The spatial distribution of boils of a given threshold (Figure 19) is very nonuniform: in the region between $x = 16h$ and $2h$ (over the latter part of the stoss side and the dune crest) the number of boils observed was much above the average value. Correspondingly, fewer boils appeared on the lee side and near reattachment. We also separated the boils that occurred for the first time from those that were present in previous realizations, and were advected from one realization to the next. The number of first occurrences is also shown in Figure 19, and also shows a nonuniform distribution. The lifetime of the boils is of the order of one or two flow-through times ($20–40h/U_b$); however, as they are advected downstream, the boils become weaker, and cannot be detected any longer with the same threshold (although they would still appear if the p' threshold is decreased).

Boils are associated with very significant transport of mass [13, 14, 21, 30], momentum and energy; this explains their importance, despite the relatively low frequency of their occurrence. Figure 20 shows one horseshoe responsible for a boil, together with contours of the local TKE, $u'_i u'_i/2$, divided by the average TKE at that location, $\mathcal{K}$. The horseshoe vortex is associated with values of the TKE 15 times larger than the mean, and values of the Reynolds shear stress $u'v'$ (not shown) over 40 times the mean value.
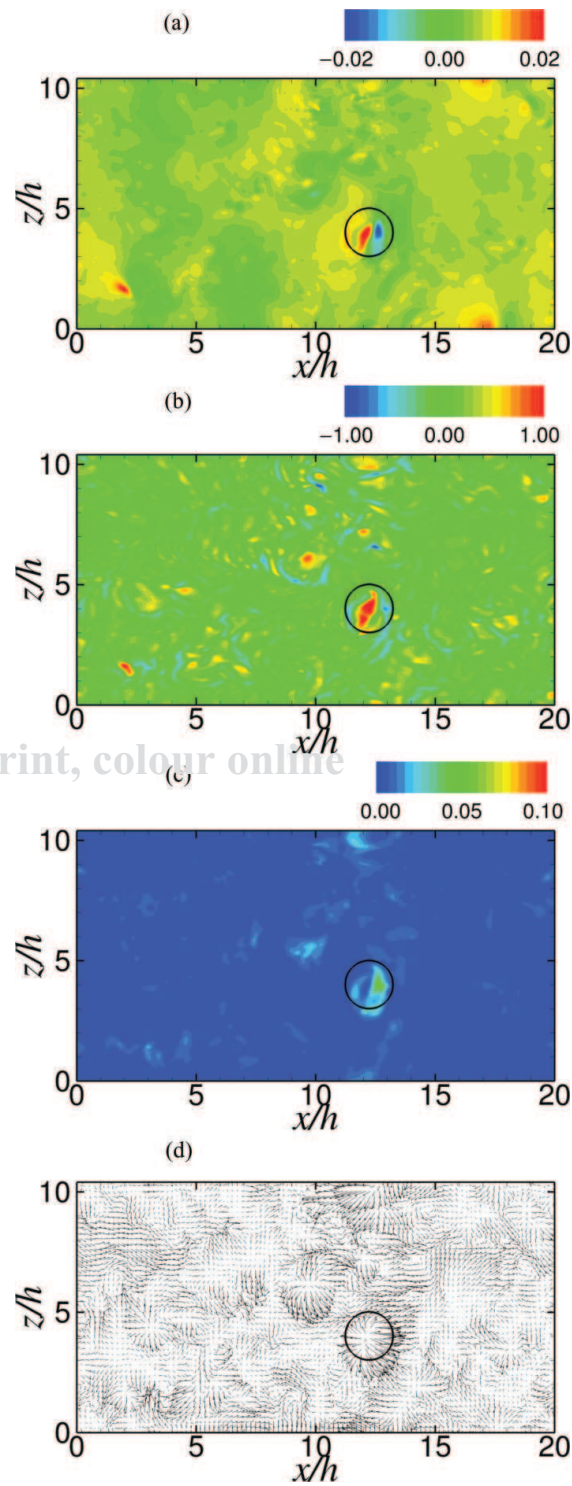
Figure 16.   Identification of a boil at the surface of flow over a flat-bed open channel using (a) pressure fluctuations p', (b) planar fluctuating velocity divergence $\partial u'/\partial x + \partial w'/\partial z$, (c) turbulent kinetic energy $\mathcal{K}$, and (d) fluctuating velocity vectors.
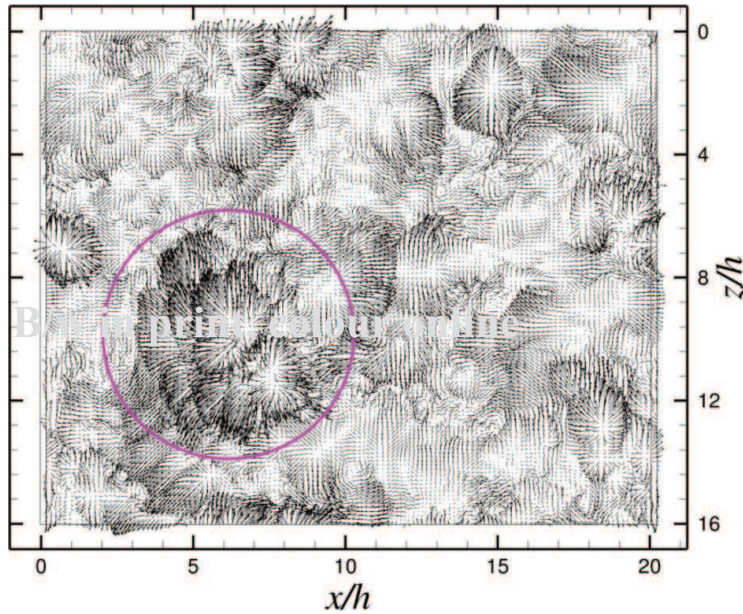
Figure 17.   Fluctuating velocity vectors at the free surface of dune geometry. The size of a boil at an instant is shown by a purple circle.

A more quantitative description of the turbulent events that occur in the flow over dunes can be obtained from quadrant analysis. We have considered the velocity fluctuation components parallel and normal to the mean-flow streamlines (which will be called u_s and u_n respectively). Following [64], in Figure 21, we show the covariance integrands of parallel and normal velocity fluctuations, $u'_s u'_n P(u'_s, u'_n)$, where $P(f, g)$ is the joint PDF of f and g, along three vertical lines at the dune crest, near the time-averaged reattachment point and on the stoss side. They are compared with the same quantities measured at homologous points (the distance to the wall normalized by local depth, D_i, being equal for the two cases) in the open-channel flow over a flat bed.

In plane channel, the near-wall behavior is dominated by the streaky structures, which result in an elongated shape of the covariance integrand (the streamwise fluctuations are larger than the wall-normal ones); a predominance of Q4 events (fourth quadrant, $u'_s > 0$
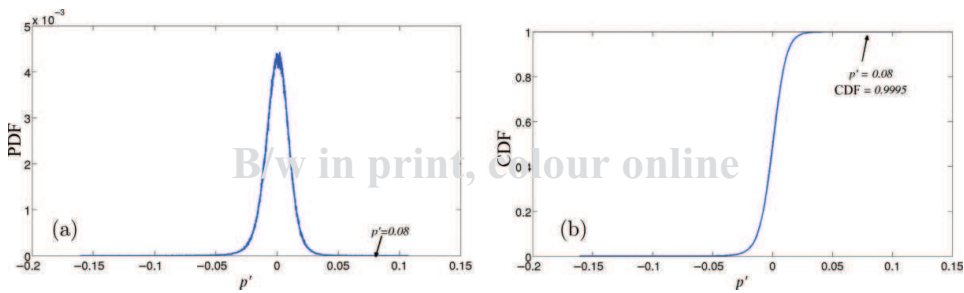

Figure 18.   (a) Probability density function (PDF) and (b) cumulative density function (CDF) of p' at the surface.
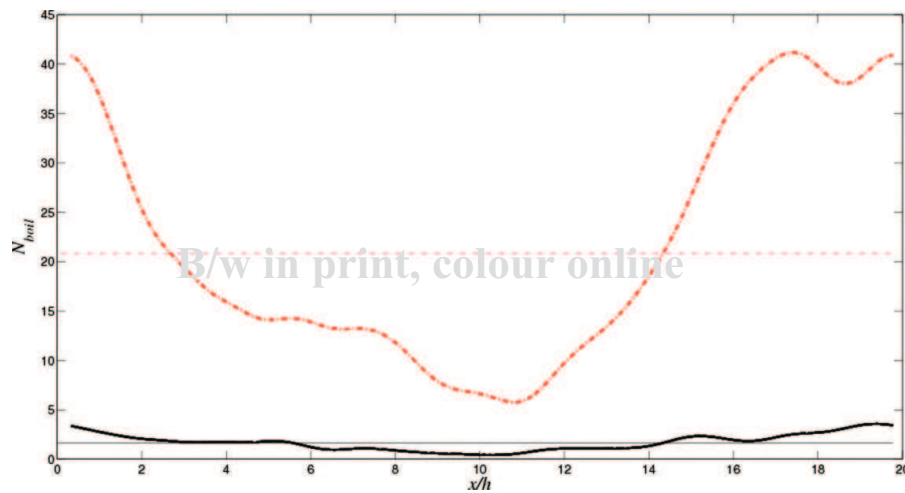
Figure 19. Number of boils observed in the computational domain over a time $1,000h/U_b$ at the surface. – – – Total boils observed; ——— boils observed for the first time. The thin lines represent the average value of the thick curve.

and $u'_n < 0$) is also expected (point 10 in Figure 21) [64]. In the dune flow, this behavior is observed in the attached flow near the crest (point 1) and on the stoss side (point 7); in the reattachment region a more symmetrical pattern is observed, due to the impingement of shear-layer eddies. While the range of wall-parallel fluctuations is the same for the flow over dunes and over a flat wall, the wall-normal fluctuations are larger by a factor of approximately two. At mid-depth (points 2, 5, 8, and 11) ejections ($u'_s < 0$ and $u'_n > 0$) are more dominant both in the plane channel and over the dunes. The range of the normal fluctuations is again larger in the dune case than for the flat-bed open channel flow, and very strong ejections are observed at points 5 and 8, which correspond to the maximum frequency of boil presence (Figure 19). These turbulent events are dominant in the shear
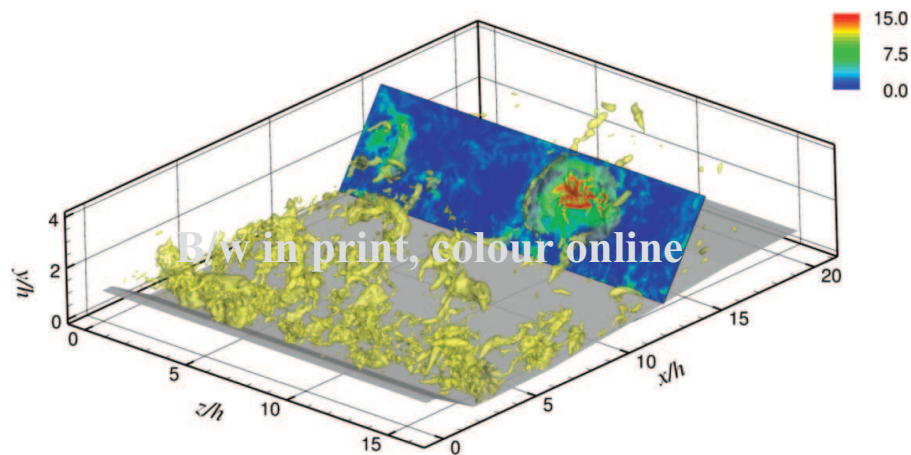

Figure 20. Isosurfaces of pressure fluctuations, and contours of the ratio of local turbulent kinetic energy to its average value at the same location.
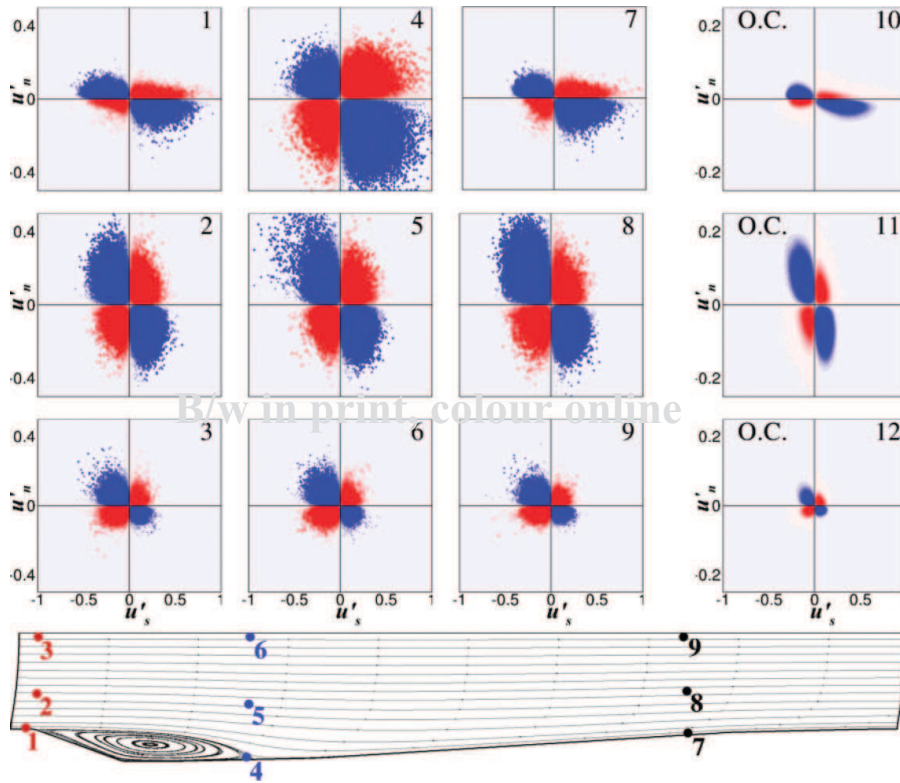
Figure 21.   Covariance integrands of u' and v'. Average distances from the wall are $0.02D_i$ for points 1, 4, 7, and 10, $0.4D_i$ for points 2, 5, 8, and 11, and $0.97D_i$ for points 3, 6, 9, and 12.

layer [10, 65]. Strong ejections are also observed at the surface, especially over the stoss side and the dune crest (points 6 and 9).

Since large coherent vortices are associated with low pressure [66], the path of the horseshoe-like vortices responsible for the boils can also be tracked by computing the probability of the instantaneous pressure being highly negative (less than $-5p_{rms}$). The number of events at which this condition is met is shown in Figure 22(a). Strong horseshoes are convected downstream and upward toward the surface, and reach the free surface at the end of stoss side. This result is consistent with the quadrant analysis shown earlier, and indicates that large boils at the surface are caused by attachment of horseshoe-like structures at the surface, and these structures are originally generated as a result of separation of the flow at the crest.

The pressure spectra at several points in the flow are shown in Figure 22(b). The Strouhal number is defined as $St = fh/U_o$, where U_o is the free-stream velocity on the crest (at $x = 0.5h$). At points 1–5, which were chosen along the crest of the probability of $p' < -5p_{rms}$ events, we observe a secondary spectral peak at $St \simeq 0.08$, which reflects the shedding frequency (as observed in studies of backward-facing step [56, 67] and previous dune flow simulations [37]). It is also in the range of the measurements by Venditti and Bauer [6] as well as the range proposed by Jackson [30], $St = 0.04 - 0.11$. Points 6–8, which are outside the path, do not have a peak at this frequency. Points 6 and 7, in the reattachment region, show a peak at a lower frequency, $St \simeq 0.065$. This result is consistent
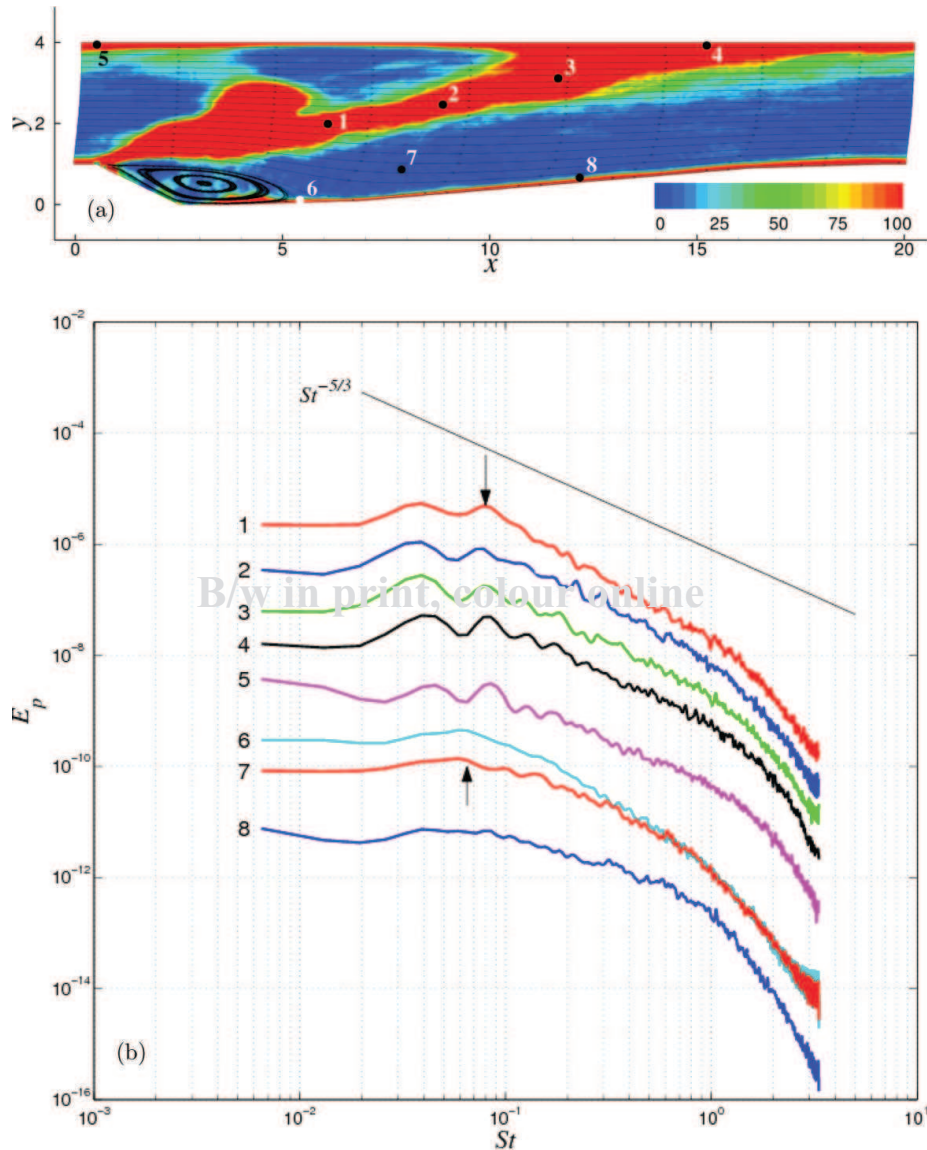
Figure 22.   (a) Contours of the number of occurrence of the event $p' < -5p_{rms}$ over 10,000 snapshots covering $1000h/U_b$ time units; (b) pressure spectra at the points marked in (a); each curve is shifted downward by a factor of 10 for clarity.

with the hypothesis that the boil-generating horseshoe vortices are generated from the vortex shedding that occurs in the separated shear layer and supports the mechanism proposed by Müller and Gyr [22], rather than the near-wall [30] or reattachment point [27] conjectures.

4.   Conclusions

We performed large-eddy simulation of the flow over two-dimensional dunes at laboratory scale (the Reynolds number based on the average channel height and mean velocity is

18,900). The mean flow separates at the crest and reattaches ~~5.2h~~ downstream on the stoss side of the dune. Overall good agreement is obtained between this simulation and experiments and simulations reported in the literature. After separation, the return-to-equilibrium is similar to that observed in other flows of this type (backward-facing step, for instance). The favorable pressure gradient on the upward slope does not play a major role in the recovery.

Turbulent kinetic energy budgets show the importance of turbulent transport and mean-flow advection at the top of the shear layer caused by the separation of the flow at the crest. In the recirculation zone and in the attached boundary layers, production and dissipation are the most significant terms in the energy budgets.

Near-wall turbulence is strongly affected by the shape of the bed after the reattachment point. Disturbances on the concave part of the stoss side cause streamwise Taylor–Gortler vortices to be generated. These vortices cause more coherent organized elongated streaks close to the wall in contrast to the streaks in turbulent boundary layer.

The flow over two-dimensional dunes has unique characteristics among open-channel flows because of the presence of spanwise vortices in the separated shear layer generated by the Kelvin–Helmholtz instability. We linked these vortices to the surface boils by an examination of instantaneous flow visualizations, quadrant analysis, and through the pressure spectra.

Flow visualizations show the birth and evolution of large eddies, which are formed when the spanwise vortices in the shear layer undergo lateral instabilities that form an inclined horseshoe-like vortex. This is also supported by power spectra and conditional sampling of the signatures of these vortices. This conclusion confirms the model proposed by Müller and Gyr [22]. Between the legs of these vortices, strong ejections occur (with $u'v'$ over 40 times and TKE over 15 times larger than the local mean). When these eddies reach the surface, the ejection causes a local stagnation point on the surface, with divergent streamlines, similar to those observed in the field when boils occur. The edges of the boil are characterized by large values of the TKE, and are much larger than those normally observed in open-channel flow over a smooth bed.

Acknowledgements

References

[1] A. Robert and W. Uhlmann, *An experimental study on the ripple-dune transition*, Earth. Surf. Proc. Landf. 26 (2001), pp. 615–629.

[2] R.J. Schindler and A. Robert, *Flow and turbulence structure across the ripple-dune transition: An experiment under mobile bed conditions*, Sedimentology 52 (2005), pp. 627–649.

[3] T. Itakura and T. Kishi, *Open channel flow with suspended sediments*, J. Hydr. Div. 106 (1980), pp. 1325–1343.

[4] J.L. Best, *The fluid dynamics of river dunes: A review and some future research directions*, J. Geophys. Res. 119 (2005), pp. 1–21.

[5] S.E. Coleman, V.I. Nikora, S.R. McLean, T.M. Clunie, T. Schlicke, and B.W. Melville, *Equilibrium hydrodynamics concept for developing dunes*, Phys. Fluids 18 (2006), p. 105104.

545 [6] J.G. Venditti and B.O. Bauer, *Turbulent flow over a dune: Green River, Colorado*, Earth. Surf. Proc. Landf. 30 (2005), pp. 289–304.

[7] S.E. Coleman and V.I. Nikora, *Initiation and growth of fluvial dunes*, in *Marine and River Dune Dynamics*, ~~D. Parsons, T. Garlan, and J. Best eds.~~, 2008, pp. 43–49.   **Q2**

[8] J. Nelson, S. McLean, and S. Wolfe, *Mean flow and turbulence fields over two-dimensional bed forms*, Water Resour. Res. 29 (1993), pp. 3935–3953.

[9] S.R. McLean, M. Nelson J., and S.R. Wolfe, *Turbulence structure over two-dimensional bed forms: Implications for sediment transport*, J. Geophys. Res. 99 (1994), pp. 12729–12747.

[10] S.J. Bennett and J.L. Best, *Mean flow and turbulence structure over fixed, two-dimensional dunes: Implications for sediment transport and bedform stability*, Sedimentology 42 (1995), pp. 491–514.

[11] M.W. Schmeeckle, Y. Shimizu, H. Baba, and S. Ikezaki, *Numerical and experimental investigation of turbulence over dunes in open-channel flow*, Monthly Rep. Civ. Eng. Res. Inst. 551 (1999), pp. 2–15.

[12] J.L. Best, *Kinematics, topology and significance of dune-related macroturbulence: Some observations from the laboratory and field*, in *Fluvial Sedimentology VII*, M.D. Blum, S.B. Marriott, and S. Leclair eds., ~~Vol. 35~~, Special Publication of International Association of Sedimentologists, Blackwell Publishing, Oxford, 2005, pp. 41–60.   **Q3**

[13] K.M. Rood and E.J. Hickin, *Suspended-sediment concentration and calibre in relation to surface-flow structure in Squamish River estuary, southwestern British Columbia*, Can. J. Earth. Sci. 26 (1989), pp. 2172–2176.

[14] R.A. Kostaschuk and M.A. Church, *Macroturbulence generated by dunes: Fraser River, Canada*, Sed. Geol. 85 (1993), pp. 25–37.

[15] R.A. Kostaschuk, *A field study of turbulence and sediment dynamics over subaqueous dunes with flow separation*, Sedimentology 47 (2000), pp. 519–531.

[16] S.R. McLean and J.D. Smith, *A model for flow over two-dimensional bed forms*, J. Hydr. Eng. 112 (1986), pp. 300–312.

[17] J.M. Nelson and J.D. Smith, *Mechanics of flow over ripples and dunes*, J. Geophys. Res. 94 (1989), pp. 8146–8162.

[18] T.B. Maddux, J.M. Nelson, and S.R. McLean, *Turbulent flow over three-dimensional dunes: 1. Free surface and flow response*, J. Geophys. Res. 108(F1) (2003).

[19] T.B. Maddux, S.R. McLean, and J.M. Nelson, *Turbulent flow over three-dimensional dunes: 2. Fluid and bed stresses*, J. Geophys. Res. 108(F1) (2003).

[20] J.G. Venditti, *Turbulent flow and drag over fixed two- and three-dimensional dunes*, J. Geophys. Res. 112 (2007).

[21] G.H. Matthes, *Macroturbulence in natural stream flow*, Eos. Trans. AGU 28 (1947), pp. 255–265.

[22] A. Müller and A. Gyr, *On the vortex formation in the mixing layer behind dunes*, J. Hydr. Res. 24 (1986), pp. 359–375.

[23] M.W. Schmeeckle, Y. Shimizu, K. Hoshi, H. Baba, and S. Ikezaki, *Turbulent structures and suspended sediment over two-dimensional dunes*, in *River, Coastal and Estuarine Morphodynamics, Proceedings International Association for Hydraulic Research Symposium*, Springer, New York, 1999, pp. 261–270.

[24] J.G. Venditti and S.J. Bennett, *Spectral analysis of turbulent flow and suspended sediment transport over dunes*, J. Geophys. Res. 105 (2000), pp. 22035–22047.

[25] D. Shugar, R.A. Kostaschuk, J.L. Best, D.R. Parsons, S.N. Lane, O. Orfeo, and R.J. Hardy, *On the relationship between flow and suspended sediment transport over the crest of a sand dune, Rio Parana, Argentina*, Sedimentology 57 (2010), pp. 252–272.

[26] I. Nezu and H. Nakagawa *Turbulence in Open-Channel Flows*, Balkema, 1993.   **Q4**

[27] A. Kadota and I. Nezu, *Three-dimensional structure of space-time correlation on coherent vortices generated behind dune crests*, J. Hydr. Res. 37 (1999), pp. 59–80.

[28] S.C. Babakaiff and E.J. Hickin, *Coherent Flow Structures in Squamish River Estuary, British Columbia, Canada*, in *Coherent Flow Structures in Open Channels*, P. Ashworth, S. Bennett, J.L. Best, and S. McLelland, eds., Wiley, 1996, pp. 321–342.   **Q5**

[29] J.L. Best, R.A. Kostaschuk, and P.V. Villard, *Quantitative visualization of flow fields associated with alluvial sand dunes: Results from the laboratory and field using ultrasonic and acoustic Doppler anemometry*, J. Vis. 4 (2001), pp. 373–381.

[30] R.G. Jackson, *Sedimentological and fluid-dynamic implications of the turbulent bursting phenomenon in geophysical flows*, J. Fluid Mech. 77 (1976), pp. 531–560.

[31] N.J. Cherry, R. Hillier, and M.E.M.P. Latour, *Unsteady measurements in a separated and reattaching flow*, J. Fluid Mech. 144 (1984), pp. 13–46.

[32] C. Mendoza and H.W. Shen, *Investigation of turbulent flow over dunes*, J. Hydr. Eng. 116 (1990), pp. 459–477.

[33] J.Y. Yoon and V.C. Patel, *Numerical model of turbulent flow over sand dune*, J. Hydr. Eng. 122 (1996), pp. 10–18.

[34] W. Yue, C. Lin and V. Patel, *Large eddy simulation of turbulent open-channel flow with free surface simulated by level set method*, Phys. Fluids 17 (2005), p. 025108.

[35] W. Yue, C.L. Lin and V.C. Patel, *Large-eddy simulation of turbulent flow over a fixed two-dimensional dune*, J. Hydr. Eng. 132 (2006), pp. 643–651.

[36] T. Stoesser, C. Braun, M. García-Villalba, and W. Rodi, *Turbulence structures in flow over two-dimensional dunes*, J. Hydr. Eng. 134 (2008), pp. 42–55.

[37] D.G.E. Grigoriadis, E. Balaras, and A.A. Dimas, *Large-eddy simulations of unidirectional water flow over dunes*, J. Geophys. Res. 114 (2009).

[38] E.A. Zedler, and R.L. Street, *Large-eddy simulation of sediment transport: Currents over ripples*, J. Hydr. Eng. 127 (2001), pp. 444–452.

[39] R. Balachandar, C. Polatel, B.S. Hyun, K. Yu, C.L. Lin, W. Yue, and V.C. Patel, *LDV, PIV and LES investigation of flow over a fixed dune*, in *Sedimentation and Sediment Transport*, A. Gyr and W. Kinzelbach, eds., Kluwer, Dordrecht, 2003, pp. 171–178.

[40] S. Kumar, R. Gupta, and S. Banerjee, *An experimental investigation of the characteristics of free-surface turbulence in channel flow*, Phys. Fluids 10 (1998), pp. 437–456.

[41] A. Leonard, *Energy cascade in large-eddy simulations of turbulent fluid flows*, Adv. Geophys. 18A (1974), pp. 237–248.

[42] M. Germano, U. Piomelli, P. Moin, and W.H. Cabot, *A dynamic subgrid-scale eddy viscosity model*, Phys. Fluids A 3 (1991), pp. 1760–1765.

[43] C. Meneveau, T.S. Lund, and W.H. Cabot, *A Lagrangian dynamic subgrid-scale model of turbulence*, J. Fluid Mech. 319 (1996), pp. 353–385.

[44] S.A. Jordan, *A large-eddy simulation methodology in generalized curvilinear coordinates*, J. Comput. Phys. 148 (1999), pp. 322–340.

[45] V. Armenio and U. Piomelli, *A Lagrangian mixed Subgrid-Scale model in generalized coordinates*, Flow Turbul. Combust. 65 (2000), pp. 51–81.

[46] C.M. Rhie and W.L. Chow, *Numerical study of the turbulent flow past an airfoil with trailing edge separation*, AIAA J. 21 (1983), pp. 1525–1532.

[47] J. Kim and P. Moin, *Application of a fractional step method to incompressible Navier–Stokes equations*, J. Comput. Phys. 59 (1985), pp. 308–323.

[48] A. Silva Lopes and J.M.L.M. Palma, *Simulations of isotropic turbulence using a non-orthogonal grid system*, J. Comput. Phys. 175 (2002), pp. 713–738.

[49] A. Silva Lopes, U. Piomelli, and J.M.L.M. Palma, *Large-eddy simulation of the flow in an S-duct*, J. Turbul. 7 (2006), pp. 1–24.

[50] S. Radhakrishnan, U. Piomelli, A. Keating, and A. Silva Lopes, *Reynolds-averaged and large-eddy simulations of turbulent non-equilibrium flows*, J. Turbul. 7 (2006), pp. 1–30.

[51] S. Radhakrishnan, U. Piomelli, and A. Keating, *Wall-modeled large-eddy simulations of flows with curvature and mild separation*, ASME J. Fluids Eng. 130 (2008).

[52] R. Balachandar, B.S. Hyun, and V.C. Patel, *Effect of depth on flow over a fixed dune*, Can. J. Civ. Eng. 43 (2007), pp. 1587–1599.

[53] P. Spalart, *Numerical study of sink-flow boundary layers*, J. Fluid Mech. 172 (1986), pp. 307–328.

[54] B.F. Armaly, F. Durst, J.C.F. Pereira, and B. Schönung, *Experimental and theoretical investigation of backward-facing step flow*, J. Fluid Mech. 127 (1983), pp. 473–496.

[55] M. Kiya and K. Sasaki, *Structure of large-scale vortices and unsteady reverse flow in the reattaching zone of a turbulent separation bubble*, J. Fluid Mech. 154 (1985), pp. 463–491.

[56] H. Le, P. Moin, and J. Kim, *Direct numerical simulation of turbulent flow over a backward-facing step*, J. Fluid Mech. 330 (1997), pp. 349–374.

[57] R.D. Moser and P. Moin, *The effects of curvature in wall-bounded turbulent flows*, J. Fluid Mech. 175 (1987), pp. 479–510.

[58] R.S. Barlow and J.P. Johnston, *Structure of a turbulent boundary layer on a concave surface*,
660   J. Fluid Mech. 191 (1988), pp. 137–176.
[59] T.S. Lund and P. Moin, *Large-eddy simulation of a concave boundary layer*, Int. J. Heat Fluid
           Flow 17 (1996), pp. 290–295.
[60] W. Gong, P.L. Taylor, and A. Dornbrack, *Turbulent boundary-layer flow over fixed aerodynam-*
           ically rough two-dimensional sinusoidal waves, J. Fluid Mech. 312 (1996), pp. 1–37.
665 [61] J. Fröhlich, C.P. Mellen, W. Rodi, L. Temmerman, and M.A. Leschziner, *Highly resolved large-*
           eddy simulation of separated flow in a channel with streamwise periodic constrictions, J. Fluid
           Mech. 526 (2005), pp. 19–66.
[62] J. Kim, P. Moin, and R.D. Moser, *Turbulence statistics in fully developed channel flow at low*
           Reynolds number, J. Fluid Mech. 177 (1987), pp. 133–166.
670 [63] R.J. Adrian, *Hairpin vortex organization in wall turbulence*, Phys. Fluids 19 (2007), p. 041301.
[64] L. Ong and J.M. Wallace, *Joint probability density analysis of the structure and dynamics of the*
           vorticity field of a turbulent boundary layer, J. Fluid Mech. 367 (1998), pp. 291–328.
[65] J.M. Nelson, R.L. Shreve, S.R. McLean, and T.G. Drake, *Role of near-bed turbulence structure*
           in bed load transport and bed form mechanics, Water Resour. Res. 31 (1995), pp. 2071–2086.
675 [66] S.K. Robinson, *Coherent motions in the turbulent boundary layer*, Annu. Rev. Fluid Mech. 23
           (1991), pp. 601–639.
[67] A. Silveira Neto, D. Grand, O. Métais, and M. Lesieur, *A numerical investigation of the coherent*
           vortices in turbulence behind a backward-facing step, J. Fluid Mech. 256 (1993), pp. 1–25.